Chapter 2

Experimental

2.1 Growth

The study of the influence of microstructure on vortex dynamics has been carried out by using Melt-Textured Grown $YBa_2Cu_3O_{7-\delta}$ samples obtained at the Department of Magnetic and Superconducting Materials in the Institut de Ciència de Materials de Barcelona. Certainly, a high maturity on the methodology of preparation and growth of these samples was required in order to achieve a controlled microstructure. Only a few years after the appearance of $YBa_2Cu_3O_{7-\delta}$ textured samples (when samples of high quality have been systematically obtained together with an important capacity to modify in a controlled way their characteristics has been achieved) this systematic study has been possible.

The importance of Melt Textured Growth processes lies in the possibility of obtaining large samples. As it has been already mentioned, the existence of grain boundaries (arising from the ceramic origin of the cuprates) represents an important issue in improving superconducting properties. Melt textured growth has enabled to avoid large angle grain boundaries leaving *only* low angle grain boundaries ($\Delta\theta < 5^o$) having a much lower influence on superconducting properties. To do so, the growth direction has to be induced by external methods. Two different methods have been used, giving place to the Top-Seeding growth and the Bridgman method. Both methods start by using an initial mixture of $YBa_2Cu_3O_{7-\delta}$ $+\alpha\%$wt of $Y_2BaCuO_5 + 1\%$wt of CeO_2 ($10 < \alpha < 30$) and compress it in the shape of pellets or cylindrical bars, respectively. The presence of Y_2BaCuO_5 enables to obtain large single domains while the presence of CeO_2 impedes coarsening of the Y_2BaCuO_5 particles which are kept down to a submicrometric size (which has been demonstrated to improve also flux pinning). The methods used in this work in order to obtain the samples studied have been:

Top Seeding Growth: The mixture is compressed in the form of a pellet, and a seed with cell parameters similar to those of $YBa_2Cu_3O_{7-\delta}$ is placed on the top of this pellet. The sample is heated to a temperature just above the peritectic temperature where the mixture is found to be in a semiliquid state (Y_2BaCuO_5 (solid)+CuO (liquid)+$BaCuO_2$
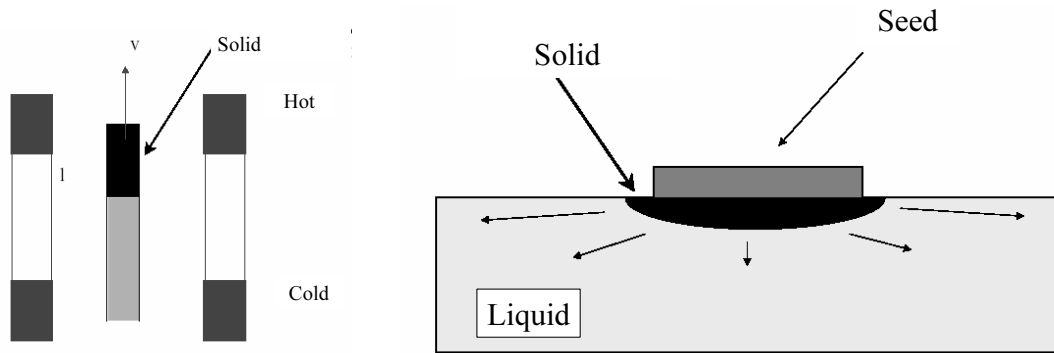
Figure 2.1: Scheme of the experimental setup used to obtain MTG-YBa$_2$Cu$_3$O$_{7-\delta}$ samples by the Bridgman method (left) and the Top-Seeding method (right).

(liquid)). Afterwards, the system is slowly cooled down in the right temperature window. If the rate of the decrease of temperature is slow enough, the mixture will solidify induced by contact with the solid with the same crystallographic orientation as the seed. Thus, the solid single domain expands through all the sample and consequently, the whole sample will grow with the crystallographic structure induced by the seed.

Bridgman method: In this case, the mixture is compressed (under isostatic pressure) as a bar. The main characteristic of this method is the use of a furnace with a gradient of temperature so that the maximum temperature obtained is slightly higher than the peritectic temperature of the mixture. The bar is placed in this furnace and slowly moved upwards. A region of the bar, the one placed on the hottest region of the furnace, is found to be in the melt state (the large viscosity of the mixture, even in the liquid state, avoids the bar from falling). As the liquid region of the bar is moved away from the zone with a maximum temperature, it starts to solidify. Different grains appear at the beginning of this process, but the different growth rate between them promotes the existence of a single grain. After this initial competition, the remaining grain induces the oriented solidification of the liquid. A large ($l \sim 8cm$, $\varnothing \sim 1cm$) single domain is therefore obtained (with the ab-plane at 60° from the long axis of the bar).

These two methods enable to obtain samples larger than single crystals with a much more complex microstructure. The Melt Textured Grown samples studied in this work have been provided by A.E.Carrillo [55] and E.Mendoza [56] of the Department of Magnetic and Superconducting Materials at the Institut de Ciència de Materials de Barcelona. The complex microstructure of MTG-YBa$_2$Cu$_3$O$_{7-\delta}$ samples, with Y$_2$BaCuO$_5$ particles, microcracks, stacking faults, dislocations, grain boundaries, twin boundaries ... has been described in section 1.4.1.

2.2   Post-processes and modifications on the preparation

In order to be able to perform a comparative study between samples with strongly different microstructural properties, different modifications of the preparation process, together with different Post-processes have been employed:

Additions of Y_2BaCuO_5 particles:
   The influence of vortex pinning in the interface $YBa_2Cu_3O_{7-\delta}/Y_2BaCuO_5$ have been widely studied in the solid vortex state, where an increase of the critical currents is associated to the enhancement of the density of extended pinning centers (i.e., $YBa_2Cu_3O_{7-\delta}/Y_2BaCuO_5$ interfaces). In order to extend this study to the liquid state, samples with different initial percentage of Y_2BaCuO_5 phase have been prepared.

Additions of $ZrBaO_3$ particles:
   Although Y_2BaCuO_5 particles are useful for vortex pinning in MTG-$YBa_2Cu_3O_{7-\delta}$, the obtention of a MTG sample without Y_2BaCuO_5 particles to be used as a reference sample is worth of consideration. This has been achieved by introducing $ZrBaO_3$ in the starting mixture [57], since $ZrBaO_3$ pushes Y_2BaCuO_5 particles during the growth, enabling the obtention of large single domains. In these single domains, Y_2BaCuO_5 and $ZrBaO_3$ appear forming large macrosegregations, widely separated and therefore, small pieces of MTG-$YBa_2Cu_3O_{7-\delta}$ without Y_2BaCuO_5 particles have been obtained. By measuring the paramagnetic signal of Y_2BaCuO_5 particles, the final content of Y_2BaCuO_5 in a small piece of one of the samples thus obtained has been determined, revealing itself consistent with the complete absence of these particles in the sample. The measurement of the temperature dependence of the critical current and the following deconvolution of the two contributions to vortex pinning also demonstrates that a very small contribution of correlated disorder, attributed to the presence of twin boundaries, exists.

Cold Isostatic Pressing:
   In this post-process, samples have been submitted to an isostatic pressure of argon of 200bar at 300°C for 4h. [58]   This treatment has been shown to increase the density of dislocations aligned within the ab-plane (and parallel to <110> in particular) while keeping the density of stacking faults almost constant.

   Magnetic measurements have shown that this enhancement on the density of dislocations leads to an increase of the critical current density mainly at low temperatures, where the influence of point-like pinning centers is more important. This post-processing has been used to study the influence of dislocations as point-like defects in the vortex liquid state.[59]

High Oxygen Pressure:
   Several samples have been submitted to a High Oxygen Pressure at the ' Instituto de

Ciencia de Materiales de Madrid'. This treatments and its influence on microstructure was widely studied as a function of the temperature (from 350ºC to 600ºC) and time (from 1h to 12h) in a pressure of oxygen of 100 bar [51, 52, 60]. It was shown that this treatment involves the creation of CuO which reacts with $YBa_2Cu_3O_{7-\delta}$ to form $YBa_2Cu_4O_8$. At initial stages of the treatment, (low temperatures / short time) $YBa_2Cu_4O_8$ develops forming fingerlike structures and strongly increases the density of dislocations from $0.7 \cdot 10^{10} cm^{-2}$ to $2.8 \cdot 10^{10} cm^{-2}$. These dislocations are mainly aligned parallel to the ab-plane at 45º from twin boundaries (coinciding with <100>). At later stages, a large density of stacking faults reducing the spacing between stacking faults down to 40nm has been observed.

Magnetic measurements revealed that these two different stages have also an important influence on the critical currents: at initial stages, the dislocations (acting as point-like defects for H∥c) promotes an enhancement of the inductive critical currents. At later stages of the treatment, however, the existence of a large density of stacking faults leads to a reduction of the critical currents.

These aligned defects, in-plane dislocations and stacking faults generated by means of oxygenation treatments at a high pressure, have been used in this thesis also to study the influence of dislocations (acting as lineal defects, i.e. for magnetic fields within the ab-plane) and stacking faults, (modifying the correlation of vortices in the c-axis direction).

Additions of silver particles:

The capability of MTG-$YBa_2Cu_3O_{7-\delta}$ samples to trap high magnetic fields promote the existence of strong magnetic forces acting on the samples, and therefore, rather good mechanical properties are required. The addition of silver particles into the starting mixture has been shown to reduce the stresses present in these samples. The redistribution of the stresses lead to a decrease in the density of the microcracks parallels to the ab-plane. For instance, the incorporation of a 20%wt of silver particles has been shown to increase the mean distance between microcracks from 1.7 to 6.7 μm [61].

Preliminary studies of the influence of microcracks suggested an enhancement of the critical current density associated to the reduction of microcrack density. However, a careful study of the microstructure and the deconvolution of the influence of point-like and linear-like pinning centers on the critical currents was required prior to any conclusion. This quantitative investigation demonstrated that the enhancement on the density of dislocations and twin boundaries as the content of silver increases is enough to explain the increase on the critical currents [51].

The study of samples with different content of silver has enabled the study of the influence of microcracks in the liquid vortex state.

2.3 Microstructural Characterization

The analysis of the relation between the microstructure and the superconducting properties required an exhaustive study of the density of each of the defects present in the sample. The densities of some of the defects present in the sample (such as dislocations or stacking faults) had already been determined [51, 61]. This determination was performed by:

- The density of microcracks was obtained by analysis of images obtained by Scanning Electron Microscopy of an ac-plane, thus enabling to determine the density of ab-microcracks in MTG-$YBa_2Cu_3O_{7-\delta}$ samples. [61]

- The density of dislocations was obtained by analyzing Transmission Electron Microscopy images of an ab-plane. It has to be noted that in a TEM image, electrons penetrate into the sample thickness ($t \sim 1000\text{Å}$), and thus a TEM image determines a volume. For each image, the length of dislocations present in each TEM image was obtained and therefore, the length of dislocations per unit volume was determined. [51]

- The density of ab-lying stacking faults has been performed by using TEM images of an ac-plane (thus perpendicular to the stacking faults). Therefore, the distance between stacking faults was obtained. [51]

However, a complete picture of the microstructure of the samples was required and therefore, the densities of Y_2BaCuO_5 particles and twin boundaries had to be also found. The procedure employed is described in the following.

2.3.1 Y_2BaCuO_5 particles

As detailed in chapter 1, the action of Y_2BaCuO_5 particles over vortices is due to its interface [47], and therefore, the area of Y_2BaCuO_5 particles has to be obtained. To do so, both, the volume fraction of the sample occupied by Y_2BaCuO_5 particles ($V = \frac{V_{211}}{V_{123}+V_{211}}$) and their mean diameter ($\langle d \rangle$) are required. These quantities have been obtained through two different methods: the volume fraction of Y_2BaCuO_5 may be obtained by magnetic measurements while their diameter requires analysis of images of MTG-$YBa_2Cu_3O_{7-\delta}$ samples.

V: Melt textured samples are composed mainly of $YBa_2Cu_3O_{7-\delta}$ and Y_2BaCuO_5 phases. From the magnetic point of view, $YBa_2Cu_3O_{7-\delta}$ (above the superconducting transition) has a temperature independent paramagnetism, while Y_2BaCuO_5 is paramagnetic and follows the Curie-Weiss law. Since the paramagnetic signal of $YBa_2Cu_3O_{7-\delta}$ is temperature independent and smaller than the temperature dependent Curie-Weiss like paramagnetic signal of Y_2BaCuO_5, when measuring the signal of MTG samples, the overall contribution will be mainly due to the paramagnetic contribution of Y_2BaCuO_5 particles.
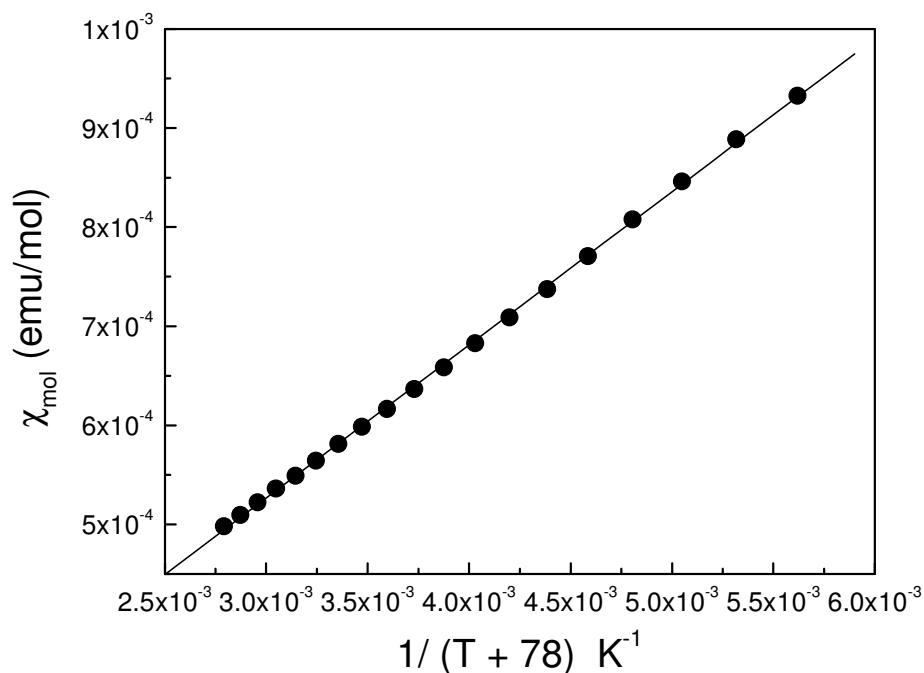
Figure 2.2: Paramagnetic signal of a MTG-YBa$_2$Cu$_3$O$_{7-\delta}$ sample with a 31%wt of Y$_2$BaCuO$_5$.

Therefore, we proceed by measuring the temperature dependence of the magnetization, for H=5T and $100K < T < 300K$ (the range of temperatures was chosen in order to avoid the influence of superconductivity). The magnetic signal thus obtained is shown in figure 2.2. There it is observed that the susceptibility ($\chi = \frac{M}{H}$) decreases with temperature. Furthermore, it follows the Curie-Weiss law:

$$\chi = \frac{C}{T - \theta_{Y211}} + \chi_0, \tag{2.1}$$

with $\theta_{Y211} \approx -78K$ and C a constant depending on the paramagnetic signal of Y$_2$BaCuO$_5$. As the signal (per unit mass of Y$_2$BaCuO$_5$) given by the particles is already known, the mass of the particles embedded in the matrix may be determined. Taking into account the theoretical densities of Y$_2$BaCuO$_5$ and YBa$_2$Cu$_3$O$_{7-\delta}$, the mass fraction is transformed into the volume fraction of Y$_2$BaCuO$_5$ in the matrix (V).

$<d>$: The determination of the size distribution of Y$_2$BaCuO$_5$ particles has been performed by analysis of images obtained by Scanning Electron Microscopy (SEM). The image analysis of the samples in order to determine the size of the particles is possible after cleaving an ab-plane and etching this surface for t=1min in 10% diluted acetic acid, in order to enhance the contrast between Y$_2$BaCuO$_5$ particles and the superconducting
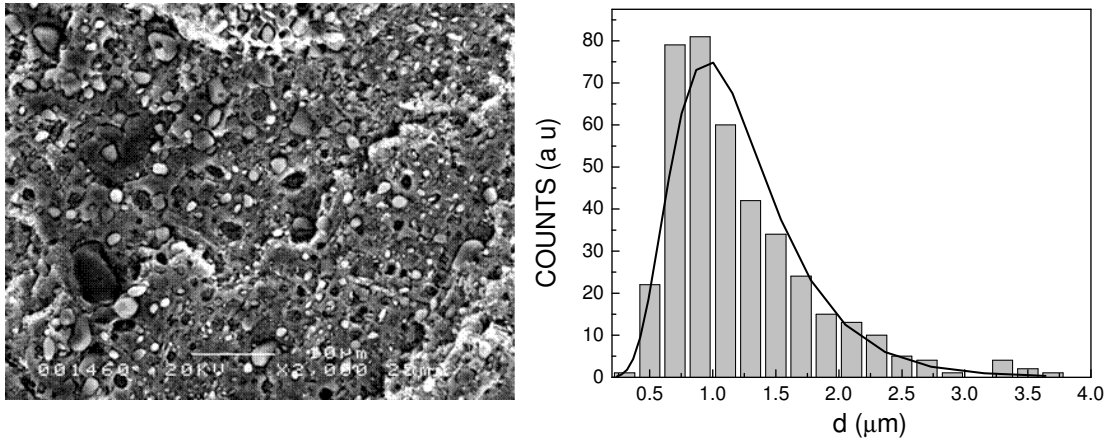
Figure 2.3: Left: image obtained by SEM of a YBa$_2$Cu$_3$O$_{7-\delta}$ sample with 31% of Y$_2$BaCuO$_5$ particles. Right: Size distribution of the Y$_2$BaCuO$_5$ particles present in this image.

matrix. In figure 2.3 (left) is shown one of the images taken in order to quantify the size of the particles. Finally, the main diameter of all the observed particles is computed, thus obtaining the size distribution of the particles (shown in figure 2.3).

This procedure has enabled us to determine the area of the Y$_2$BaCuO$_5$/YBa$_2$Cu$_3$O$_{7-\delta}$ interface (per unit volume): $a \propto \frac{V}{\langle d \rangle}$. The quantity $V/\langle d \rangle$ will be the parameter employed to measure the influence of the Y$_2$BaCuO$_5$ particles.

2.3.2 Twin Boundary density

The determination of the density of twin boundaries has been performed by image analysis of the samples. Two different sources for the images have been employed:

TEM: Several images were obtained by Transmission Electron Microscopy (TEM) of the ab-plane from each sample. As seen in figure 2.4left, twin boundaries are determined as the interface between regions having different contrast, which arises from the small differences existing between the a and b-axis.

SEM: In order to obtain images by Scanning Electron Microscopy (SEM) with enough contrast across twin boundaries, an ac-plane has to be observed (2.4right). Furthermore, the observed surface has to be etched (1min in 10% diluted acetic acid, similarly to the treatment to observe Y$_2$BaCuO$_5$ particles) after polishing.

Another item has to be considered when determining the distance between twin boundaries since the observed plane is an arbitrary plane parallel to the c-axis. The observed apparent distance (d_{exp}) needs to be accordingly projected: if the plane is parallel to one of the
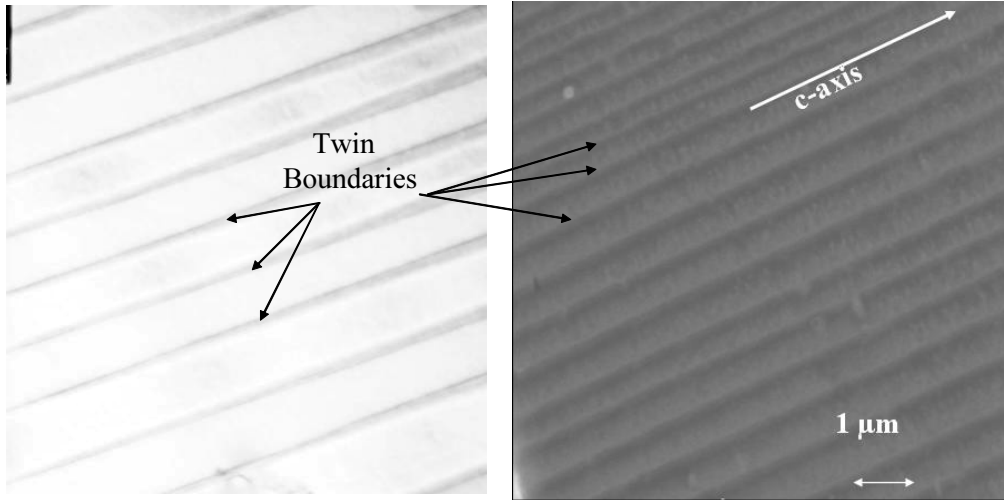
Figure 2.4: Left:TEM and Right: SEM image of MTG-YBa$_2$Cu$_3$O$_{7-\delta}$ samples. Arrows indicate the twin boundaries.

two twin boundary families, this family will produce an infinite apparent distance, while for the other family the apparent distance will correspond to the exact distance. For an intermediate direction ($\alpha \sim 45^o$ degrees from each family), the observed distance will be equal for both families, but slightly larger than that of twin boundaries. This influence is schematically shown in figure 2.5.

In general, for a particular angle, α, between twin boundaries and the plane parallel to the c-axis, we obtain:

$$d_{TB} = \frac{d_{exp}}{2} \cdot (\cos \alpha + \sin \alpha), \qquad (2.2)$$

where α is the angle between the twin boundaries and the observed ac-plane and d_{exp} the main observed distance, i.e. the weighed average between d$_1$ and d$_2$. Equation 2.2, for $\alpha \approx 45^o$ becomes $d_{TB} \approx \frac{\sqrt{2}}{2} \cdot d_{exp}$, thus the distance between twin boundaries is a 35% lower than observed when considering an ac-plane at 45°. Observation of the ab-plane using an optical microscope with polarized light (near the edge of the samples) enables to determine the angle (α) between twin boundaries and the edge of the sample.

The analysis of these pictures has enabled us to obtain the distribution of distances between twin boundaries, for all the samples considered. This distribution is shown in figure 2.6 for two particular samples. The average distance between twin boundaries within a sample is observed to vary from $\langle d_{TB} \rangle \approx 580$Å to $\langle d_{TB} \rangle \approx 4700$Å, i.e. a variation of nearly one order of magnitude, enabling to quantify the modification of the superconducting properties with the density of twin boundaries.
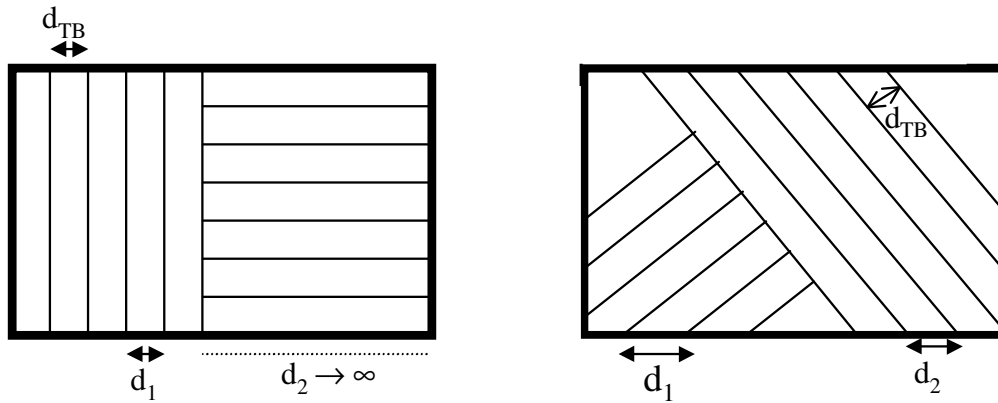
Figure 2.5: Scheme of two different samples (the surface corresponds to the ab-plane) showing the influence of the relative orientation of twin boundaries on the observed distance between twin boundaries.
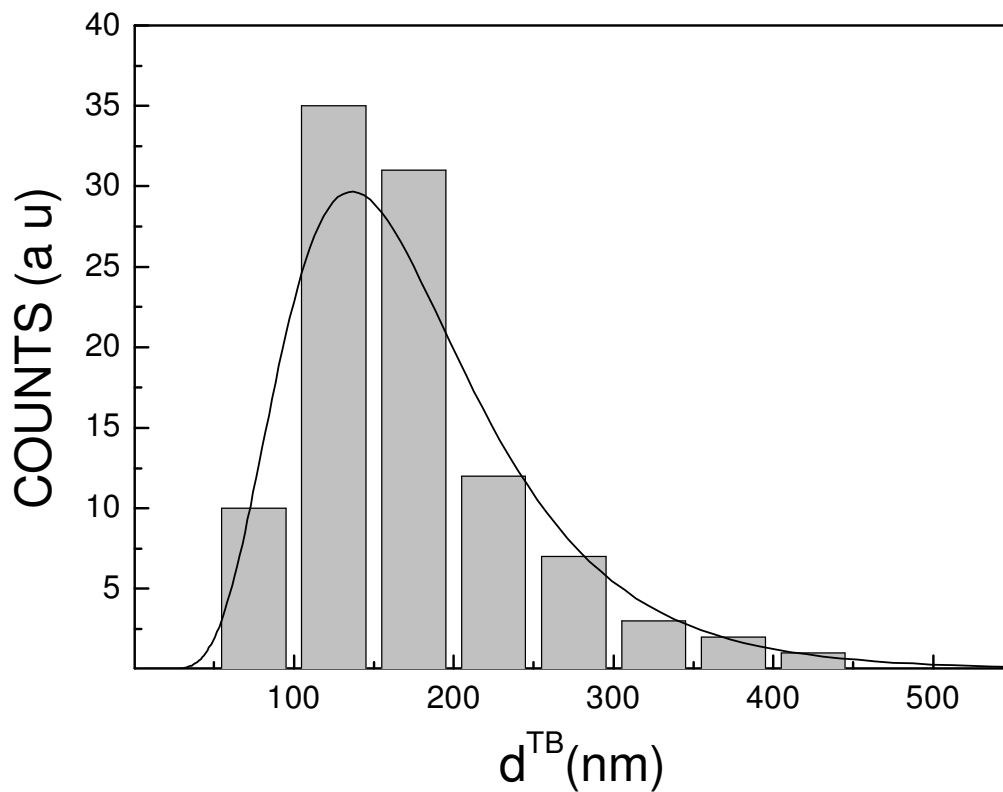

Figure 2.6: Distribution of twin boundaries spacing in a MTG-$YBa_2Cu_3O_{7-\delta}$ sample.

SAMPLE	Y_2BaCuO_5 % wt	V/d (cm^{-1})	Ag_2O % wt	d_{micro} (μm)	d_{SF} (nm)	d_{TB} (nm) (nm)	σ_{disl} (cm^{-2})
0%Y211	0t	0	0	—	—	470	—
18% Y211	18	2000	0	1.7	—	125	—
31% Y211	31	3300	0	—	—	170	—
10% Ag_2O	18	2000	10	3.7	—	83	—
20% Ag_2O	18	2000	20	6.7	—	51	—
CIP	31	3300	0	—	—	—	up to 10^{11}
HOP(disl)	31	3300	0	—	—	—	$2 \cdot 10^{10}$
HOP(SF)	31	3300	0	—	~ 38	170	—

Table 2.1: Microstructural characteristics of the samples studied in this thesis. Shown is the content of Y_2BaCuO_5, their interface density, the content of Ag_2O and the distance between microcracks and twin boundaries. Post-processing has been carried out by CIP (Cold Isostatic Pressing), HOP whit short treatment (HOP(disl)) and long time and high temperature (HOP(SF)).

2.3.3   Summary of the Microstructural Characteristics

Once the experimental determination of the microstructural properties has been explained, it is certainly worth to show clearly the microstructural characteristics of the samples that are studied in this work. Thus, the volume fraction of Y_2BaCuO_5 particles, their interface density, the content of silver, the distance between twin boundaries, the distance between microcracks, the distance between stacking faults and the density of dislocations for these samples are shown in table 2.1.

Although the complex relations between the different defects on MTG-$YBa_2Cu_3O_{7-\delta}$ samples is far beyond the goal of this work, it is certainly worth mentioning the strong modification of the density of twin boundaries (about one order of magnitude), simply by modifying the content of secondary phases. Firstly, it is observed in table 2.1 that the distance between twin boundaries decreases as the content of silver is enhanced from 0% to 20%. The origin of the enhancement of the density of twin boundaries (and that of dislocations [51]) has to be related to the reduction in the density of microcracks, promoting an enhancement of the stresses to be absorbed in the matrix.

On the other hand, as it arises from the values of table 2.1, the density of twin boundaries follows a nonmonotonic dependence with the content of Y_2BaCuO_5 particles. It was argued [62] that the distance between twin boundaries increases with the size of the subgrains. However, the size of the subgrains in the present samples is unknowk, and thus, a further insight is not possible.

2.4 Superconducting Properties

The diversity of defects present in MTG-YBa$_2$Cu$_3$O$_{7-\delta}$ samples requires to check whether their influence on the superconducting properties is detrimental or not. In order to investigate this influence, two different experimental approaches have been followed: inductive and resistive measurements.

2.4.1 Inductive Measurements

In the mixed state of a type II superconductor, with a certain density of microstructural defects, the penetration of vortices is determined by vortex pinning. Therefore, a non-uniform distribution of vortices (and a gradient of magnetic field) is generated, which in turn promotes a force over vortices. In the critical state, this force is equal to the pinning force.

By means of the study of the magnetization induced at different magnetic fields and temperatures, the inductive critical currents, directly related to the strength of vortex pinning, can be extracted. These critical currents are directly related to the strength of vortex pinning, and therefore, to the pinning centers. Furthermore, it was demonstrated that critical currents due to point-like defects[16] and linear-like defects [17] have different temperature dependencies. Taking into account the whole $J_c - T$ curve, the contribution from these two kinds of defects may be extracted for each sample[52] (see chapter 1).These measurements have been performed in a commercial cryostat M*agnetic* P*roperty* M*easurement* S*ystems* (MPMS) by Quantum Design. This cryostat operates at magnetic fields up to 5.5T and temperatures down to 4.2K. In a hysteresis cycle at a fixed temperature (see figure 2.7) the difference between the magnetic moment as increasing the magnetic field (m^-) and the magnetic moment as decreasing the magnetic field (m^+) is directly related to the strength of pinning and thus the critical current density. Therefore, we may obtain the critical current density from magnetic measurements and extract information about vortex pinning in the vortex solid state.

The analysis of the influence of the different defects on the vortex solid state is beyond the objective of this thesis (and already studied by J.Plain [51]). However, these measurements have been used to control and test the quality of the samples. It has also enabled to check whether there is a strong influence of the defects introduced by the different post-processes and treatments in the vortex solid state, prior to the sample characterization by means of resistive measurements.

2.4.2 Resistive Measurements

Sample Preparation

The samples chosen to be measured by magnetoresistance have been cut down in a parallepiped form with a larger surface of the order 1mm x 0.5 mm, which, except where noted, coincides with the ab-plane. Afterwards, and in order to enhance the sample resistance (and the sensibility of the measurements), the sample has been polished down to a thickness of
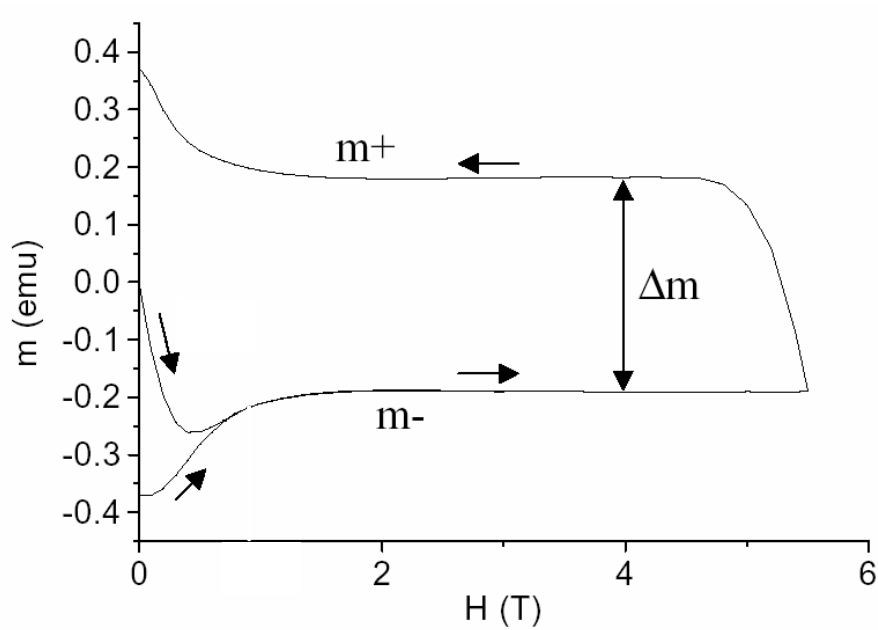
Figure 2.7: Hysteresis cycle for a MTG-YBa$_2$Cu$_3$O$_{7-\delta}$ sample at T=45K. Shown are the magnetic moment as increasing (decreasing) the magnetic field m^- (m^+) and its difference (Δm) [51].
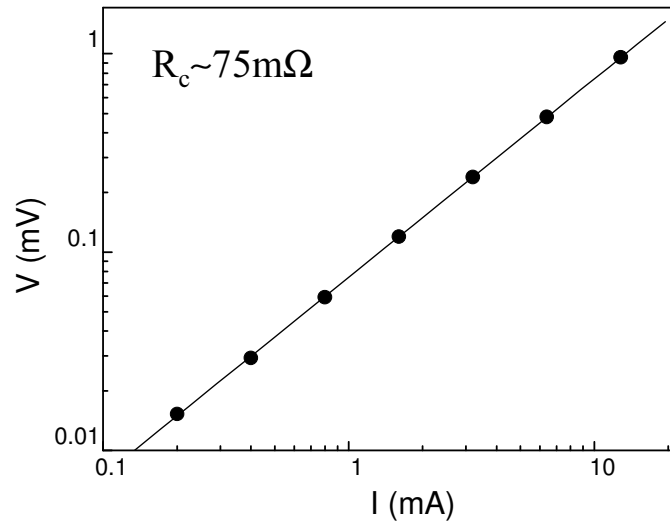
Figure 2.8: Contact resistance determination at T=77K. With this method, the resistance of the electric contact is determined as the slope of the I-V curves.

$t \sim 200\mu m$. The roughness is reduced below $1\mu m$ enabling to observe with polarized light the sample, and check the direction of twin boundaries respect to the edges of the sample. The larger edge of the sample was aligned at 45º from twin boundaries.

The sample resistivity has been determined by the 4 probe method. In this method, a current is applied through the external electrical contacts. This current circulating in the sample generates a certain dissipation between the voltage contacts. Finally, this dissipation is measured with the aid of an external detecting system.

Good quality electrical contacts where obtained by sputtering gold or silver on the pads of the contacts. A mask, superimposed on the top of the sample was used while performing the sputtering. After sputtering, the sample was submitted to an annealing temperature of T=300ºC during t=1h, under 1 bar of flowing oxygen to ensure that no oxygen is lost from the sample. Afterwards, 4 platinum wires are attached to the pads by using silver epoxy, and the previous thermal treatment is repeated in order to remove the organic part of silver epoxy, leading to a metallic contact between the sample and the wire. Contact resistances better than 0.2Ω, measured by the three points method at temperatures below the critical temperature (see figure 2.8), have been obtained.

Finally, the sample has been mounted into the sample holder by using *GE* varnish (from General Electric). The wires have been connected to the pins in the sample holder by means of silver paint. The geometry of the assembly is chosen so that the subsequent rotation of the sample adapts to our needs for each particular experiment.

ICMAB

The standard resistivity measurements carried out during this work, have been performed in a commercial equipment: a P*hysical* P*roperty* M*easurement* S*ystem* (PPMS) from Quantum Design.

After sample mounting, the sample holder is placed into a sample rotometer and inserted in the internal chamber of the cryostat. The temperature in this chamber is controlled by the flux of helium that enters into the inset and a resistance that heats the system. R-T measurements have been performed increasing the temperature at a typical rate $\frac{\Delta T}{\Delta t} \sim 0.5 \frac{K}{min}$. Comparison between measurements performed while heating or cooling revealed no significant difference.

The magnetic field, ranging from H=0T to H=$\pm$9T, is generated by a superconducting coil. The electrical current that creates the magnetic field is introduced through a superconducting switch. When the magnetic field has to be modified, the superconducting switch is heated, and an external source of current is able to modify the electrical current circulating through the magnet. The resistive measurements have been performed in a sample rotometer capable of modify the relative direction of the magnetic field.

Electrical measurements are performed using a resistance bridge that enables to determine the resistance of the sample over a large range of values. The electrical current may be changed from 1μA to 5 mA. The current has been modified in order to ensure that the measurements where performed in a linear regime. The typical current densities used are in the order of $J \sim 1 A/cm^2$. The typical noise level is found to be equivalent to voltages in the range of 10nV.

Flux Transformer Measurements

The same experimental equipment may be used in order to determine the existence of full vortex correlation across the sample in MTG-YBa$_2$Cu$_3$O$_{7-\delta}$ samples. To do so, an inhomogeneous current is applied to the sample by using two pads at the top of the sample (see figure 2.9). This inhomogeneous distribution promotes a different Lorentz force acting over vortices at the top and the bottom of the sample. Thus, it could be expected a lower motion at the bottom and therefore $V^{top} > V^{bot}$. However, if full vortex correlation is still preserved across the sample, vortex motion at the top of the sample will lead to vortex motion at the bottom of the sample, and $V^{top} = V^{bot}$. Flux transformer measurements have been performed at magnetic fields from H=0T to 9T rotating from the c-axis to the ab-plane.

Argonne National Laboratory

As it has been mentioned in section 2.2, the dislocations created, either by Cold Isostatic Pressing or High Oxygen Pressure, are aligned within the ab-plane. Therefore, the study of its influence as linear pinning centers, should be performed while rotating the magnetic field within the ab-plane. However, a straight forward attempt to measure the angular dependence of the in-plane magnetoresistance using the equipment previously described, with a single rotometer, demonstrated that any small misalignment of the sample leads to the presence
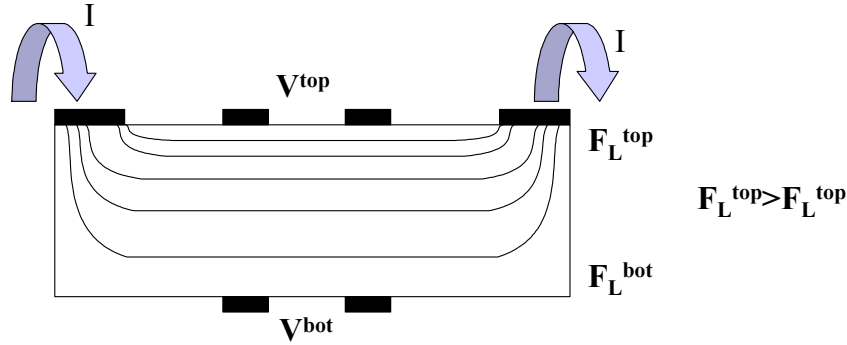
Figure 2.9: Scheme of the configuration of the flux transformer experiments. Shown is the inhomogeneous distribution of current, and the voltage at the top and the bottom of the sample.

of a component of the magnetic field parallel to the c-axis of the sample. Moreover, since the crystallographic structure is highly anisotropic, the c-axis component has a strong effect (for instance, a misalignment of 3° between the magnetic field and the ab-plane, leads to an increase of the effective magnetic field $\frac{\Delta H_{eff}}{H_{eff}} \sim 7\%$, and thus a modification larger than 1K in the obtained irreversibility line at H=9T).

An additional problem appears, related to the fact that the rotation axis of the sample may not be perfectly aligned with the c-axis: the component of the magnetic field parallel to the c-axis will change when the magnetic field is rotated. This variation will lead, therefore, to a modification of the resistivity with the direction of the magnetic field. In figure 2.10 even far from the minima of the resistivity related to twin boundaries ($\varphi = 0, 90^o$) the resistivity is not isotropic. This anisotropy is not related to the microstructure but to a change on the effective magnetic field.

In order to extract this contribution, while still rotating the sample within the ab-plane, another degree of freedom is then required. A cryostat provided with, either, crossed fields and a sample rotometer or two rotometers has to be used. Such a device exists in the facilities of the Materials Science Division in the Argonne National Laboratory (U.S.A.), where these measurements could be carried out in collaboration with Dr.K.Kwok. A scheme of this cryostat is found in figure 2.11, together with the particular geometry of this experiment. Unfortunately, since the axis of rotation of the system is parallel to the longitudinal field, H_L ($H_L^{max} = 8T$), we are unable to rotate this magnetic field within the ab-plane and to perform these measurements, we will have to rotate the transversal field, H_T ($H_T^{max} = 1.5T$) within the ab-plane and use H_L to avoid the presence of a c-axis component. Therefore, we have used low magnetic fields with $|H| \leq 1.5T$, and taking into account that it is an ab-plane magnetic field, we are restricted to effective magnetic fields $H_{eff} = \varepsilon_\theta H \leq 0.2T$. The measurements, consequently, will be performed at high temperatures, just below T_c.
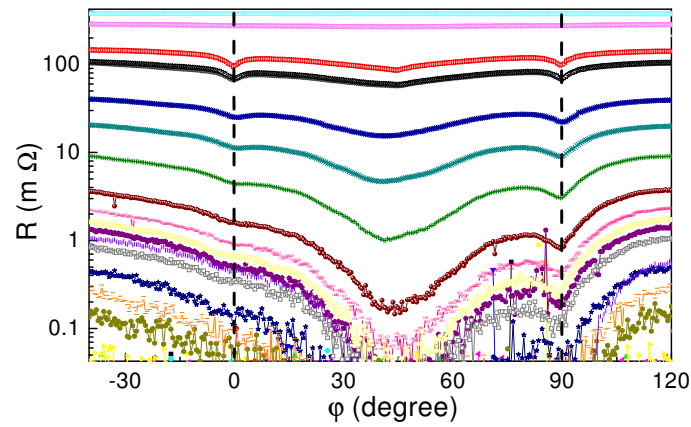
Figure 2.10: Angular dependence of the resistivity while rotating the magnetic field, nearly, within the ab-plane.The dashed lines show the directions of twin boundaries, corresponding with a local minimum on the dissipation.
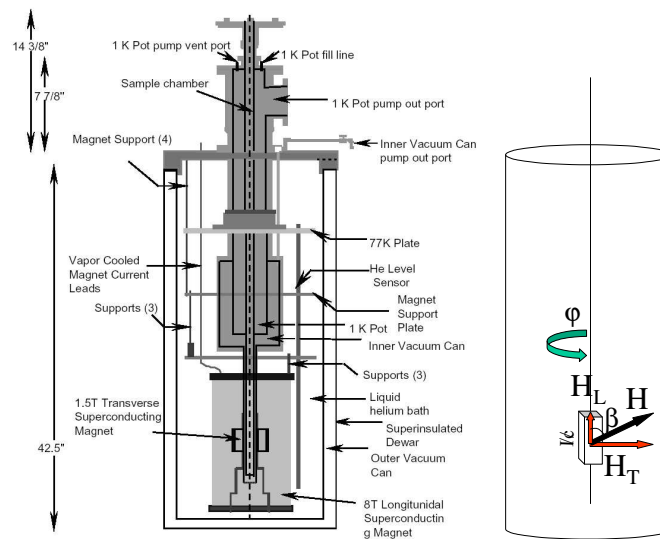

Figure 2.11: Left: Scheme of the cryostat employed in these measurements. Shown are the two superconducting magnets enabling the compensation of the magnetic field. Right: Representation of the experimental setup, showing the direction of the current and the angle β between the rotation axis and the magnetic field, and φ, the angle of rotation.
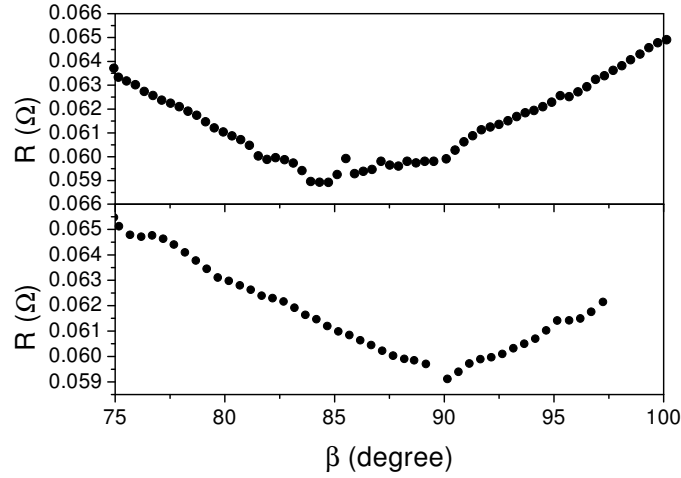
Figure 2.12: Dependence of the resistivity at H=1.5T and T=90K for a MTG-YBa$_2$Cu$_3$O$_{7-\delta}$ sample for two different φ.

In order to perform these measurements, a systematic methodology has to be employed:

1. Each direction of the sample (see figure 2.11) defines an angle φ between the transversal magnetic field and the twin boundaries. For each one, the direction of the magnetic field (β) that produces the smaller c-axis component (β_{min}) has to be found, while keeping the modulus of the magnetic field constant.

   This particular direction of the magnetic field is determined by taking into account that the system is anisotropic, and therefore, applying the magnetic field parallel to the ab-plane has to lead to a minimum in the resistivity.

   However, an enhancement of vortex pinning due to aligned defects could lead to an anomalous behavior of the angular dependence of R(β). In order to avoid any misleading effect from vortex pinning from the oriented defects, these measurements have been performed at temperatures with $\rho(T) > \rho_n/2$, where linear defects have been shown not to modify vortex dynamics. This angular dependent behavior is shown in figure 2.12, where it is observed the presence of the minimum of the resistivity, for two different orientations of the sample. The position of this minimum enables us to define, for each particular orientation of the sample (φ), the direction of the magnetic field that corresponds with the ab-plane of the sample (β_{min}). In figure 2.12, it is observed that for each particular orientation of the sample, the direction of the magnetic field that produces an in-plane magnetic field (β_{min}) is modified.

   This dependence of β_{min} with φ is represented in figure 2.13, where is shown to follow a sinusoidal dependence, as expected from geometrical considerations. This dependence of $\beta_{min}(\varphi)$ was the responsible of the anisotropic background in the previous
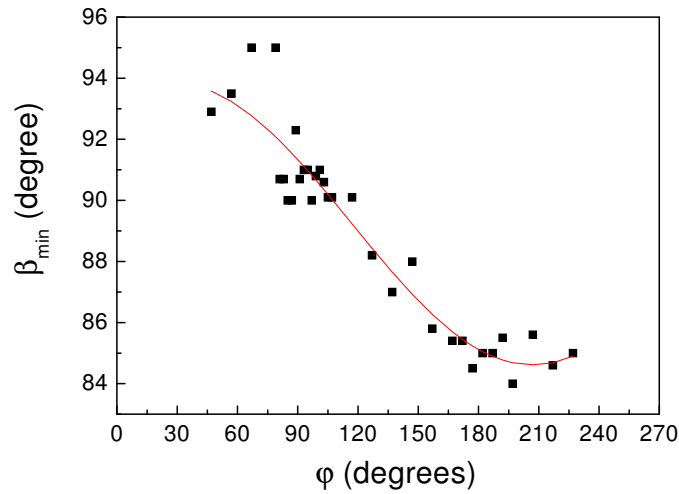
Figure 2.13: Dependence of β_{min} with φ.

measurements (see figure 2.10). $\beta_{min}(\varphi)$ has been also seen to be independent of the modulus of the applied field.

2. Once determined $\beta_{min}(\varphi)$, we have measured the temperature dependence of the resistivity $\rho(T, H, \beta_{min}(\varphi))$. The temperature has been determined and controlled by means of a Lakeshore 91C controller. Sample heating is produced by a resistance wired around a metallic cylinder that wraps the sample while the cooling is determined by the transfer of heat from the sample to the helium bath. Since the heat transfer is controlled by the vacuum in the chamber between the sample and the helium container, an improvement of the vacuum slows down the rate of decrease of temperature.

Chapter 3

Magnetoresistive Measurements.

3.1 Introduction

Vortex matter in HTSC is strongly sensitive to the large thermal, pinning and elastic energies, that exist in this system. The competition between these interactions, pointing to rather opposite behaviors and dynamics, leads to a very complex phase diagram (see section 1.2), which is still, not fully understood. Furthermore, Melt Textured Grown samples has a very rich microstructure, and therefore, the study of the influence of microstructure on vortex motion on these samples, the goal of the present work, requires a systematic methodology that enables to distinguish and quantify the role of each one of the main defects present in these samples. The methodology employed has been the following:

1. The density of each one of these defects has been systematically modified while keeping the rest of their microstructural characteristics (almost) unchanged. This procedure has finally allowed us to distinguish between the effects of defects with the same dimensionality. A quantitative determination of the density of defects present in each sample has also been performed.

2. The study of the phase diagram and vortex dynamics in the vortex liquid state by means of magnetoresistive measurements. The analysis of the angular dependence of these measurements enables to distinguish the contribution of defects with or without a preferential orientation.

In the present chapter, different HTSC systems will be analyzed, enabling us to introduce the main concepts to be used in this thesis and the principal features of the phase diagram. It will be analyzed a clean, twinned $YBa_2Cu_3O_{7-\delta}$ single crystal, where two main defects are to be considered (twin boundaries and oxygen vacancies); a Melt Textured $YBa_2Cu_3O_{7-\delta}$ sample, where the difference in the microstructural characteristics lead to changes in vortex statics and dynamics compared to that of the twinned single crystal. These changes will be pointed out. Finally, we will extend this study to two different compounds with a crystallographic structure similar to $YBa_2Cu_3O_{7-\delta}$: $NdBa_2Cu_3O_{7-\delta}$ and $YBa_2(Cu_{1-x}Mg_x)_3O_{7-\delta}$.

Both, the anisotropy (between the ab-plane and the c-axis) and vortex dynamics will be characterized in these systems.

3.2   Single crystal YBa$_2$Cu$_3$O$_{7-\delta}$: a reference

3.2.1   Solid-Liquid Transition

A highly pure, twinned YBa$_2$Cu$_3$O$_{7-\delta}$ single crystal, grown on BaZrO$_3$ crucibles by the self-flux method and oxygenated at 650° during 125h in an oxygen pressure PO$_2$=100bar has been provided by the Department de Physique de la Matière Condensèe (Université de Genève). The existence of a low density of defects in this sample [63] suggested that it would be useful to use it as a reference for the following study of MTG-YBa$_2$Cu$_3$O$_{7-\delta}$ samples with a much higher diversity and density of defects. However, twin boundaries are still present in this sample, and they are expected to be the main source of pinning in the sample, for magnetic fields nearly parallels to the c-axis. Due to these microstructural characteristics, this sample has been used to study vortex motion in the liquid state by means of resistivity measurements [32, 64].

In figure 3.1, it is shown the temperature dependence of the resistivity of the sample for different intensities of the magnetic field. At zero magnetic field, it is observed a sharp drop of the resistivity as decreasing the temperature. This sharp decrease of the resistivity (at H=0T) defines the critical temperature of the sample, i.e. the temperature at which the material becomes superconducting. We will define the superconducting temperature as the midpoint of the transition at H=0T, thus obtaining T_c =93.1K±0.4K.

At non-zero magnetic fields, however, the origin of the dissipation is vortex motion. Therefore, magnetoresistive measurements show up to be an interesting tool to study vortex dynamics, since they enable to determine whether vortices are moving or not. A vortex submitted to a small enough pinning potential, in the presence of a vanishingly small current, will move, while vortices that are submitted to a strong pinning potential, i.e. are pinned, do not move, and thus distinguish a vortex liquid state from a vortex solid state. These two scenarios are distinguished by the dissipation of the system since in the first case a finite, linear, resistivity is obtained while the second case will lead to zero resistivity, or, from the experimental point of view, a resistivity which is below our experimental resolution, as seen in figure 3.1. In magnetoresistance measurements, to use current densities high enough so that the Lorentz force is larger than the pinning force, i.e., $F_L > F_{pinning}$ would force vortex motion even in the solid state, so we will restrict ourselves to low electrical currents; in order to be in the linear regime.

In figure 3.1, it is observed that the solid-liquid transition displaces to lower temperatures as the magnetic field increases, as expected when it is considered that dissipation is related to vortex motion. However, the temperature dependence of the curves is also modified when the magnetic field is increased, thus showing the existence of two kinds of transitions from
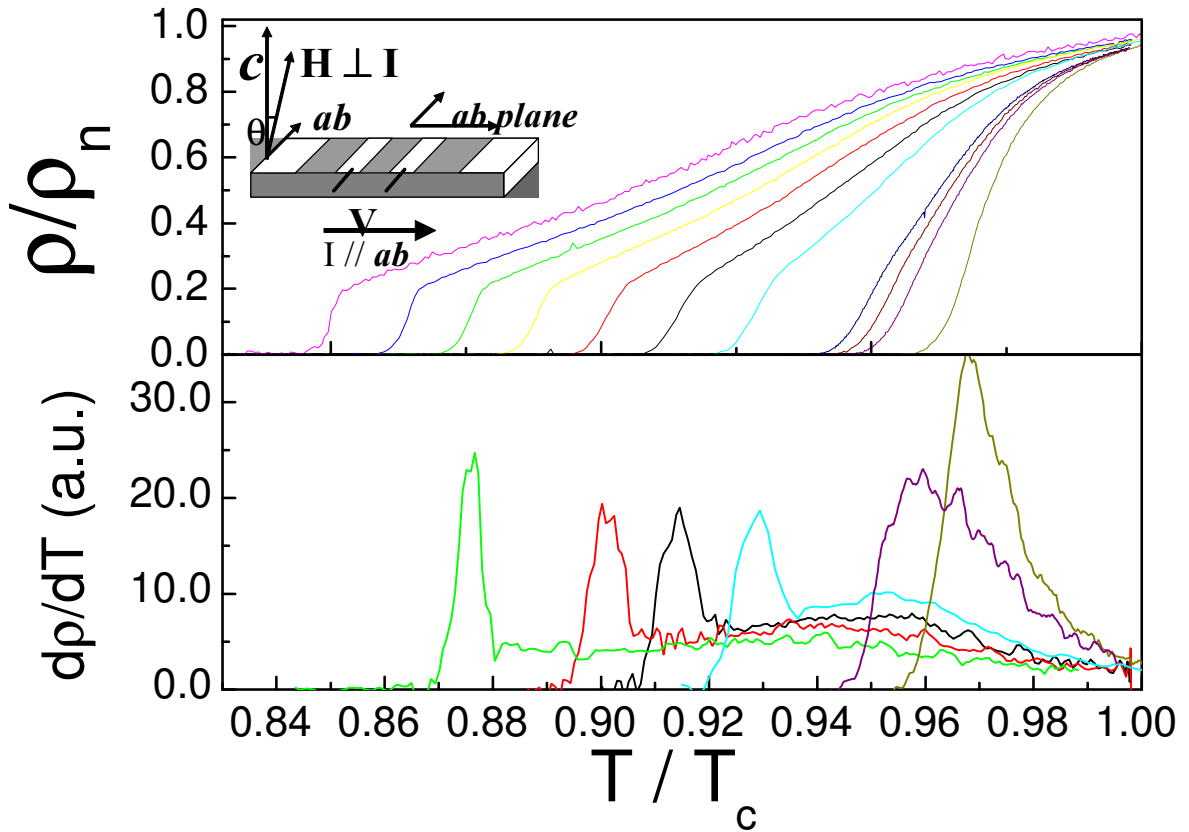
Figure 3.1: Up:Temperature dependence of the resistivity for the YBa$_2$Cu$_3$O$_{7-\delta}$ single crystal at different intensities of the magnetic field (H=0.5,1,1.4,1.8,3,4,5,6,7,8 and 9T) and θ=15° from the c-axis (away from the influence of twin boundaries). In the inset is shown the geometric configuration most commonly used in this work. Down: Derivative of the temperature dependence of the resistivity for H=0.5,1,3,4,5 and 7T.

the solid vortex state (characterized by a vanishingly small resistance) to the liquid vortex state, clearly differentiated in figure 3.1: at low magnetic fields (below H=1.5T), there is a broad, continuous transition from the normal state to the solid vortex state, while, at higher fields (above 2T) there is a sharp decrease of the resistivity from $\rho \sim 0.2\rho_n$ to a resistivity below our experimental resolution. These two different behaviors are separated by the so-called low critical point (above which the solid-liquid transition is a first order transition and below this transition becomes a second order transition). The low critical point reflects [65] the existence of two different solid states, namely, a disordered system at low fields and a vortex lattice at higher fields.

The origin of these two different phases at low temperatures is given by the predominance of either, vortex-vortex interaction which favors a long-range ordered structure or vortex pinning, that introduces disorder and destroys the vortex lattice. The different dependence with field and temperature of the related energies leads to the introduction of an ordered and a disordered phase. Thus, the existence of different interactions over vortices leads to a complex phase diagram, with two different solid phases. Following, we will study the nature of the solid-liquid transition above and below the critical field and the angular dependence of the critical point.

Melting transition

As already mentioned, the melting line is defined by the equilibrium between the thermal energy and vortex-vortex interaction. At this temperature the vortex lattice is destroyed. In a wide diversity of solid ordered systems it has been seen that one may use the Lindemann criteria [66] that determines the melting of the lattice. By expanding this empirical criteria to the melting of the vortex lattice, it melts when the thermal fluctuations of vortices around their position of equilibrium ($\langle u \rangle_{th}$) would overcome a given fraction of the intervortex distance:

$$\langle u^2 \rangle_{th}(T_m) \approx c_L^2 a_0^2, \tag{3.1}$$

where c_L is the Lindemann coefficient, $c_L \approx 0.1 - 0.3$. By introducing in equation 3.1 the temperature dependence of $\langle u^2 \rangle_{th}$ it has been obtained [10, 67] that the melting line is given by:

$$H_m = H_m(0)\left(1 - \frac{T}{T_c}\right)^\alpha, \tag{3.2}$$

with $H_m(0) = \frac{c_L^4 \Phi_0^5 \gamma^2}{12\pi k_B^2 T_c^2 \mu_0^2 \lambda_{ab}^4}$ being a parameter determined by the intrinsic properties of the sample. Moreover, since YBa$_2$Cu$_3$O$_{7-\delta}$ is anisotropic but still a 3-D compound, following the scaling approach of G.Blatter [12], we may consider that the relevant magnitude is given by the effective magnetic field $H_{eff} = \varepsilon_\theta H$, with $\varepsilon_\theta = \sqrt{\gamma^2 \cdot \sin^2(\theta) + \cos^2(\theta)}$, valid for mod-
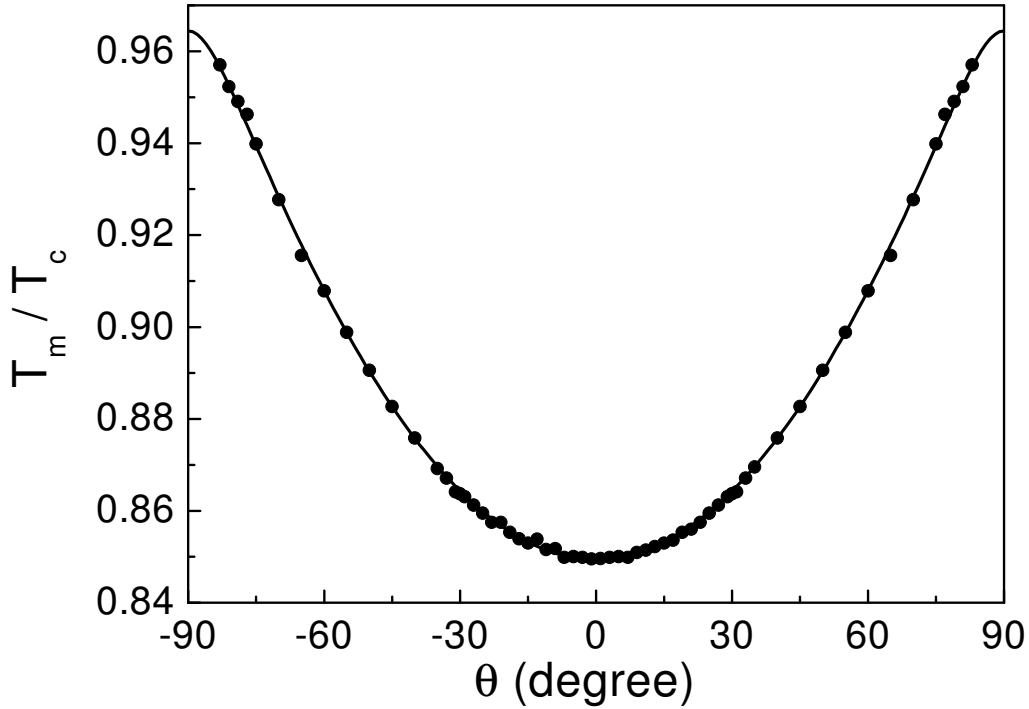
Figure 3.2: Angular dependence of the melting temperature at H=9T when rotating H from the c-axis to the ab-plane. The solid line is the fit of the experimental data to equation 3.3.

erately anisotropic superconductors. Consequently:

$$\varepsilon_\theta H_m = H_m(0) \cdot \left(1 - \frac{T}{T_c}\right)^\alpha \tag{3.3}$$

which may be checked by performing sets of R-T curves at different angles and magnetic fields.

The melting temperature has been defined as the high-temperature peak onset of $d\rho/dT(\theta, H)$[68] which is also identified as the high-temperature point where the second derivative of the resistivity reaches a zero value. By considering a fixed value of the applied magnetic field and rotating it from the c-axis to the ab-plane, we are able to obtain the angular dependence of the melting line, shown in figure 3.2. In this figure, it is observed, firstly, that as the magnetic field approaches the ab-plane, the transition temperature increases, following the anisotropy of the sample. Secondly, it is also observed that the melting line is not defined for angles higher than 84°, showing that the lower magnetic critical point (H$_{lcp}$) depends on the direction of the applied field (this angular dependence will be further studied later on).

The angular dependence of the melting line is demonstrated by adjusting T$_m(\theta)$ to equa-

tion 3.3. This fit enables us to obtain the anisotropy of the sample $\gamma^{-1} \approx 7$, in good agreement with the values obtained in the literature $\gamma^{-1} \sim 5 - 8$ [10]. It is also in good quantitative agreement with the dependence of the anisotropy with the oxygen content in $YBa_2Cu_3O_{7-\delta}$, as reported by Langan et al.[67]. We also have $\alpha \approx 1.33$ and $H_0 = 111.24T$. This value of $H_m(0)$, using $\lambda_{ab} = 1400\text{Å}$ enables us to estimate the Lindemann number, $c_L \approx 0.21$, also in good agreement with the results reported in the literature for a wide diversity of systems (see, for instance [10] and references therein).

Moreover, we are able, also, to investigate the dependence $T_m(\theta, H)$ for different applied fields in figure 3.3, where the melting line in the magnetic phase diagram for different directions of the magnetic field is shown. These curves follow the same behavior than the data of figure 3.2, since equation 3.3 adjusts to this data (without any free parameter) when using the parameters obtained from figure 3.2. This good agreement is demonstrated by representing T_m as a function of H_{eff}, in the inset of figure 3.3. The scaling of the melting line at different directions of the magnetic field, simply by considering the effective magnetic field further reinforces that the melting line is not influenced by aligned pinning centers such as twin boundaries. This behavior is actually to be expected since the melting temperature requires a low temperature ordered state where the disordering effect of the defects is overcame by the vortex-vortex interaction.

Irreversibility line

The melting line, however, is not defined for all the applied magnetic fields, since the relative importance of the disorder existing in the sample increases as decreasing the magnetic field (which reduced the vortex-vortex interaction). At low fields, therefore, the solid-liquid transition is determined by the softening of the interaction between vortex and pinning centers. This change from a first order to a second order transition as increasing the influence of disorder has already been observed in $YBa_2Cu_3O_{7-\delta}$ single crystals where a higher amount of point-like pinning centers are generated through e^- irradiation and destroys the low temperature ordered phase. [26] In systems where a certain amount of disorder is present, and contrasting to what was observed previously for the melting line, an influence of the pinning centers is expected. To observe this influence, we determine the angular dependent irreversibility line, obtained using the criteria $\rho(T_{irr}) = \frac{1}{1000}\rho_n$, with ρ_n the normal state resistivity. This criteria will be used throughout the thesis.

In figure 3.4, it is shown the angular dependent irreversibility line at H=1T. It appears clearly that, for angles higher than a certain θ_{acc} (the limit of influence of twin boundaries), the angular dependence of the transition temperature follows the intrinsic anisotropy of the sample, since the experimental data has been fitted to:

$$\varepsilon_\theta H_{irr} = H_0 \left(1 - \frac{T}{T_c} \right)^\alpha, \tag{3.4}$$

by analogy to equation 3.3. The fitting parameter H_0, however is not an intrinsic parameter,
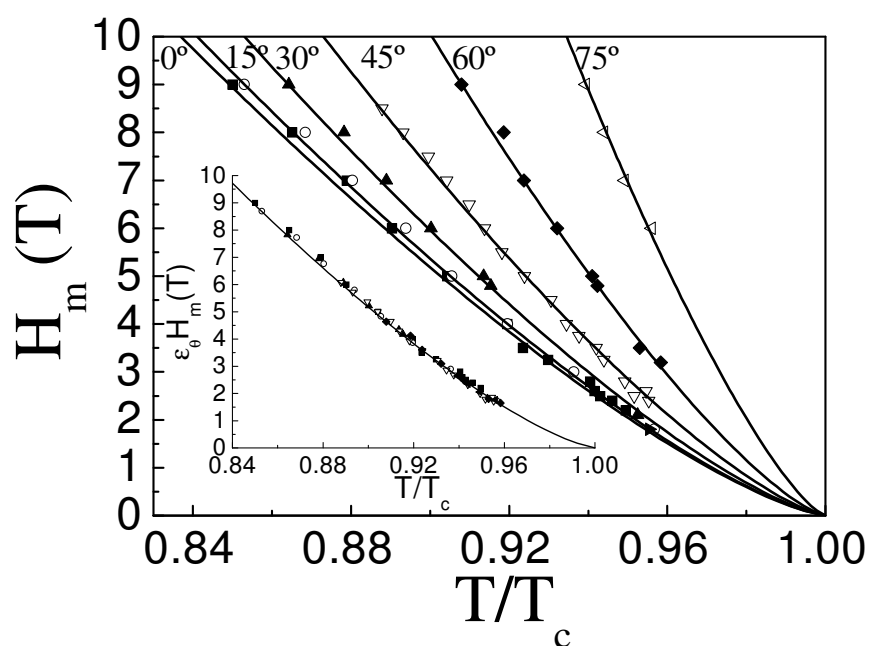
Figure 3.3: Temperature dependence of the melting field for different directions of the magnetic field. The solid lines are given by equation 3.3, using the values obtained from figure 3.2. In the inset it is shown the scaling of this data using the effective magnetic field.
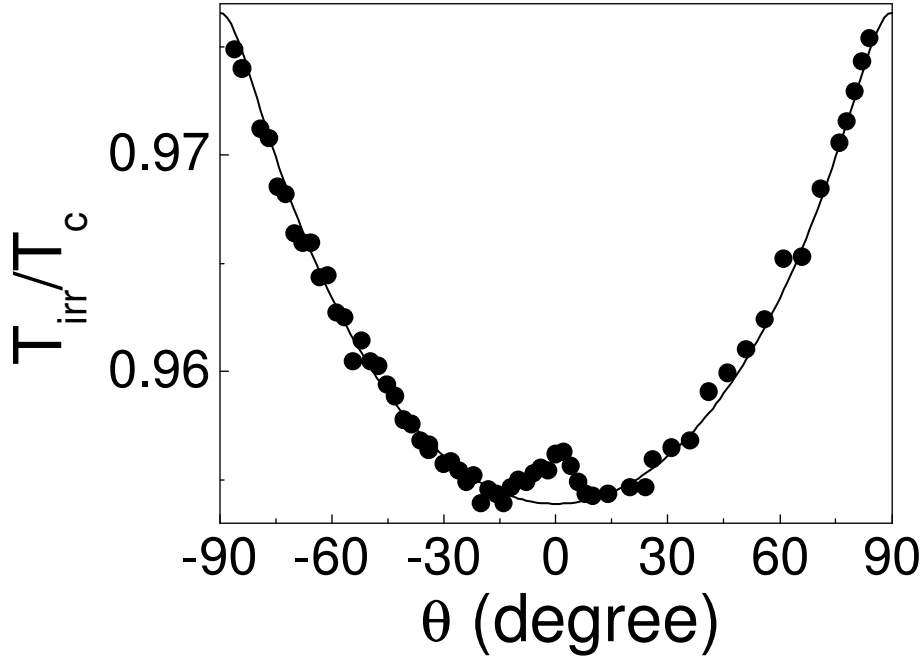
Figure 3.4: Angular dependence of the phase diagram for H=1T, and therefore, $H < H_{lcp}$.

and may be strongly modified by vortex pinning, and consequently by the particular microstructural characteristics of the sample considered. The evolution of this fitting parameter as the microstructural characteristics are modified will be used in this thesis to investigate its influence on vortex statics and dynamics.

On the other hand, for angles lower than $\theta < 15^o$, there is an upwards shift of the irreversibility line as approaching H∥c ($\theta = 0^o$). This effect, has been studied theoretically for the case of 1-D, linear defects, with analogy to the trajectory of superfluid bosons [17, 69], and attributed to the enhancement of vortex pinning at these columnar defects. At low fields, the solid-liquid transition is determined by the softening of vortex pinning and therefore, its strength (and so the presence of twin boundaries) has a strong influence in the position of the solid-liquid transition. At higher fields, the solid-liquid transition is determined by the softening of the vortex lattice and therefore, vortex pinning plays no role in the position of this transition.

Therefore, the angular dependence of T_{irr} shows that twin boundaries have an important effect on the irreversibility line, that one has to be avoid or extract in order to determine which is the contribution of the non-aligned defects present in the sample. The extrapolation to H∥c of the angular behavior allows us to obtain the properties of vortex motion without the influence of twin boundaries. By comparing both results, we will be able to obtain also the shift of T_{irr} related to twin boundaries ($\Delta T_{irr}^{TB} = T_{irr}^{TB} - T_{irr}^{bg} \approx 0.2K$ at H=1T). The experimen-

tal shift of the solid-liquid transition associated to twin boundaries will be compared over the Melt Textured samples studied in order to investigate the influence of the microstructure to ΔT_{irr}^{TB}.

Low critical point

As already mentioned, the existence of a first order and a second order transition is related to the different balance between the elastic energy and the pinning energy above and below the lower critical point. Therefore, the critical point where the first order transition becomes a second order transition is determined by the equilibrium between the three energies existing in this scenario, the thermal energy, the elastic energy and the pinning energy. The same R-T sets used previously, either varying the applied magnetic field or its direction, has enabled us the determination of the nature of the transition from the solid to the liquid, i.e. a first order or a second order transition. The angular dependence of the low critical field is shown in figure 3.5, where, it is observed that the low critical point behaves similarly to the angular dependent irreversibility line: an increase of the low critical point with θ for angles higher than 20° and an increase of the low critical point when approaching the c-axis for angles lower than 20°.

In order to understand this behavior, we have to take into account that the low critical field derives from the existence of a certain amount of disorder. Therefore, as approaching the c-axis, for $\theta < 20^o$, the disorder increases (twin boundaries act as pinning centers for these directions of the magnetic field), and so does the pinning energy. Consequently, the disordering effects become dominant over the vortex-vortex interaction which favors a vortex lattice. Therefore, the region with a second order transition expands to higher magnetic fields, leading to an enhancement of the low critical point. As approaching the ab-plane, the effective magnetic field decreases and so does the effect of vortex-vortex interaction. Therefore, a higher applied magnetic field is required to reach the equilibrium between vortex-vortex interaction, vortex pinning and the thermal energy. At angles near H∥c, there is an enhancement of the influence of disorder since for these directions vortices are pinned at the twin boundaries distorting the vortex lattice. Again, the equilibrium between these two interactions is reached at higher fields.

Certainly, a clean single crystal (i.e. with a low density of defects) is required in order to be able to observe and determine the low critical point. In melt-textured samples, having a strong influence of disorder (twin boundaries, dislocations, Y211 particles, stacking faults, microcracks...), the measurements reveal that there is not a first order transition in the region of the phase diagram studied, as will be seen in the next section.

3.2.2   Vortex dynamics

Above the solid-liquid transition, and due to the strong thermal energies involved, the effect of the pinning potential is softened, although a pinned vortex liquid, with an important
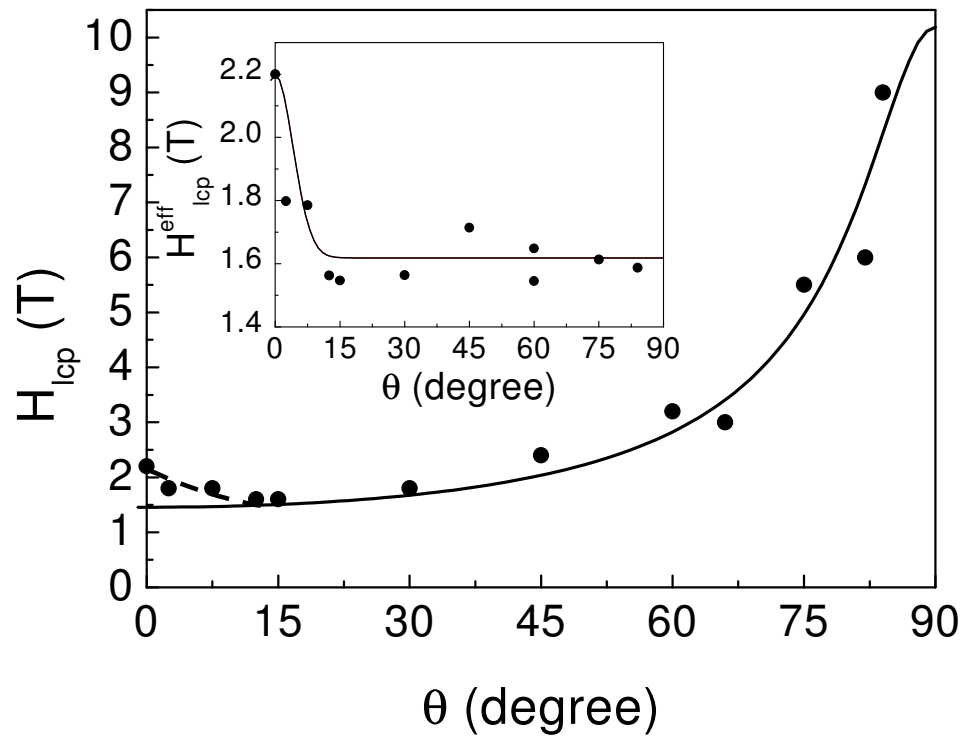
Figure 3.5: Angular dependence of the low critical field of a twinned single crystal. Inset: Angular dependence of the effective low critical field.
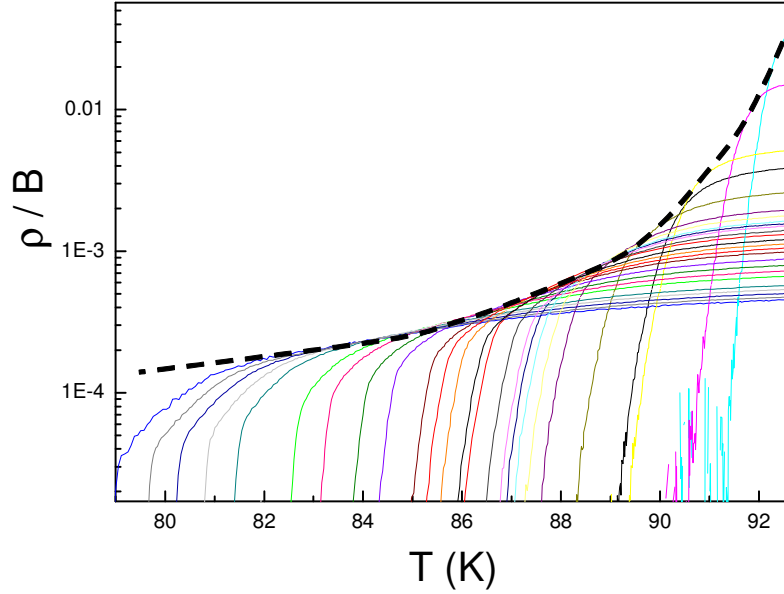
Figure 3.6: Temperature dependence of the ratio $\frac{\rho}{B}$ for H||c at H=0.1, 0.25, 0.5, 0.75, 1, 1.25, 1.5, 1.75, 2, 2.2, 2.4, 2.6, 2.8, 3, 3.25, 3.5, 3.75, 4, 4.5, 5, 5.5, 6, 6.5, 7, 7.5, 8, 8.5 and 9T. Dashed line gives the temperature dependence of the upper limit of $\frac{\rho}{B}$.

influence of vortex pinning is to be expected above the solid-liquid transition. At higher temperatures, as the pinning potential becomes much smaller than the thermal energy, vortices are not influenced by pinning centers and vortex motion follows the flux-flow model. Within the flux flow model, and for magnetic fields much lower than the upper critical field, the flux flow resistivity [3] is expressed as:

$$\rho_{ff}(T) = \rho_n(T)\frac{B}{\eta B_{c_2}(T)}, \tag{3.5}$$

where $\eta \sim 1.45$ is a constant[70]. Therefore, if it is the dominant mechanism, we have that $\frac{\rho_{ff}(T)}{B\rho_n(T)} \neq f(B)$, where $\rho_n(T)$ is determined from the extrapolation to temperatures below T_c of the normal state resistivity. The scaling of the resistivity curves when considering $\frac{\rho(T)}{B \cdot \rho_n}$ becomes apparent in figure 3.6 where the temperature dependence of this ratio is represented for different intensities of the magnetic field. It is observed that there is an upper limit of this ratio, which depends on the temperature. The temperature dependence of this saturation value is given by the dashed curve in figure 3.6. Following the flux-flow model, the temperature dependence of this limit is directly related to the upper critical field.

In order to clarify this behavior, and determine in which regions flux-flow is dominating vortex motion from this figure, we proceed by determining, at different temperatures the dependence of $\frac{\rho(T)}{\rho_n B}$ with the magnetic field, which is shown in figure 3.7. Two different regimes
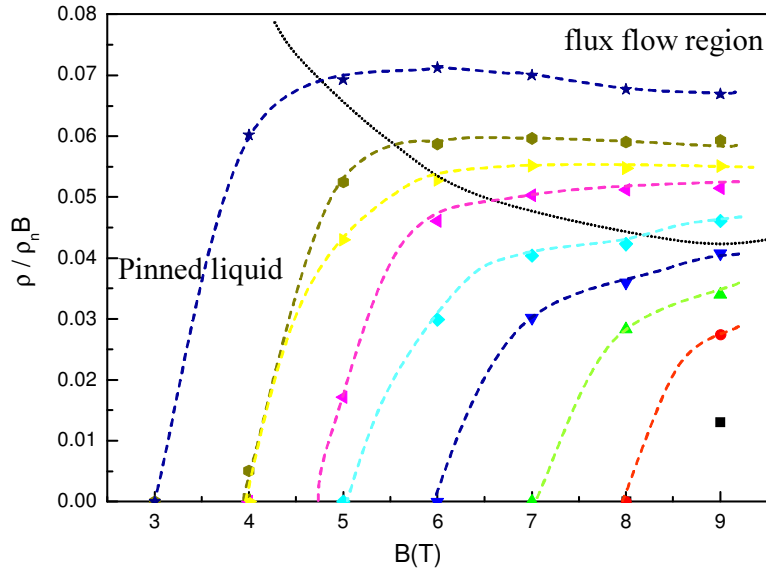
Figure 3.7: Magnetic field dependence of the ratio $\frac{\rho(T)}{\rho_n B}$, for $\theta = 15^{\circ}$ and temperatures from T=0.85T_c (lower curve) to T=0.92T_c (upper curve).

are observed in these curves, depending on the temperature and the magnetic fields, distinguished by the dashed line. Below the dashed line, a strong influence of the magnetic field is observed for each particular temperature, while, at higher temperatures (above T=85K), it is observed that this ratio is field independent at large magnetic field, in agreement with equation 3.5. Above this curve, then, vortex motion follows the flux flow model, while, at lower temperatures, a certain influence of vortex pinning is still present and it is obtained a lower resistivity than that predicted by the flux flow model while at lower temperatures an important influence of pinning centers is still present. Furthermore, the actual value of saturation obtained in the upper region of the figure, enables to estimate the upper critical field and so the temperature dependence of $B_{c_2}(T)$ is obtained.

These two behaviors enable us to obtain two different regions in the liquid region of the phase diagram, namely, a region where vortex motion is reduced by vortex pinning and a region where the resistivity is only determined by flux flow. These regions are represented in figure 3.8. In this figure, we observe the evolution of vortex motion as increasing temperature: the solid becomes a liquid (at T_{irr} or T_m) with influence of pinning. If we further increase the temperature, the influence of pinning disappears at T_{ff}, and finally, the normal state is reached at B_{c_2}. Certainly, the value of B_{c_2} has to be considered only as a rough estimation (for instance, the strong influence of fluctuations should be taken into account), and thus, the temperature dependence of the obtained upper critical field is not linear as should be expected. However, there is a good qualitative agreement with the data found in the literature [71].
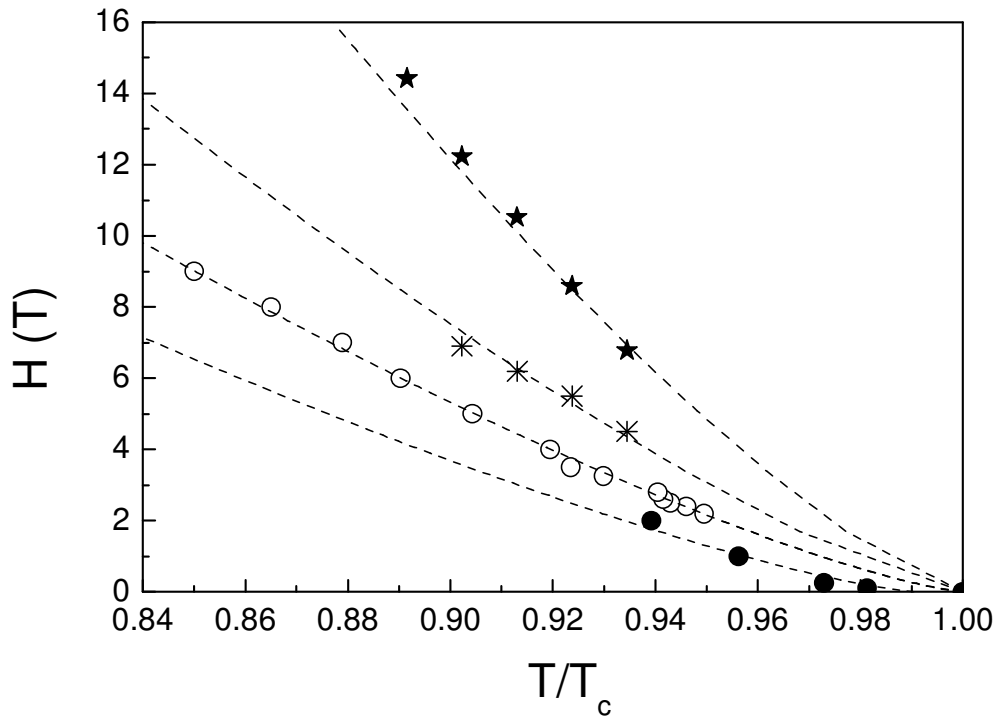
Figure 3.8: Magnetic phase diagram for H∥c. Shown are the irreversibility line (•), the melting line (○), the lower limit of the flux flow regime (×) and the upper critical field (⋆). A value η = 1.45 has been assumed in order to determine the upper critical field. Dashed lines for the melting line and the irreversibility line are the fit to equation 3.2. Dashed lines for the lower limit of the flux flow regime and B_{c_2} are guide to the eye.

This magnetic phase diagram, with three different regions of the magnetic phase diagram, namely, the vortex solid; a region with a certain influence of vortex pinning and finally a region without any influence of pinning, and the possible evolution of these regions while modifying the microstructural characteristics of the samples will be the main issue of the present work.

3.3   MTG-YBa$_2$Cu$_3$O$_{7-\delta}$

3.3.1   Phase Diagram

Melt-Textured samples, however, have strongly different microstructural characteristics to those of single crystals, due to the differences in the conditions of preparation and growth. The measurements of the temperature dependence of the resistivity in a melt textured sample; the analysis of these curves and comparison with the results obtained in a clean YBa$_2$Cu$_3$O$_{7-\delta}$ single crystal will enable us to determine the main similarities and dissimilarities between the superconducting properties of both kinds of samples, and relate them to their different microstructure.

In order to perform this comparison, Melt Textured YBa$_2$Cu$_3$O$_{7-\delta}$ samples have been grown by the Top-Seeding Method, as described in section 2.1. As mentioned previously, the main microstructural difference between MTG-YBa$_2$Cu$_3$O$_{7-\delta}$ samples and YBa$_2$Cu$_3$O$_{7-\delta}$ single crystals is the presence of Y$_2$BaCuO$_5$ particles, that enables to grow single domains (with the presence of low angle grain boundaries) with dimensions of several cm which are much larger than those of YBa$_2$Cu$_3$O$_{7-\delta}$ single crystals.

In figure 3.9, it is shown the zero-field resistivity transition of the present sample, that enables to define the critical temperature of the sample, $T_{c_0} = 89.95K$ as the onset of resistivity. There are also shown the resistive transitions for H∥c at different values of the applied magnetic field, broadening with increasing the magnetic field. If we compare these curves with those of the twinned single crystal, it is observed that no signature of a first order transition appears in this sample. This feature contrasts with the results obtained in clean single crystals, where a first order transition may be observed as increasing the temperature. In melt-textured samples, the high density of microstructural defects leads to a stronger influence of this disorder and the long range order is destroyed. This disappearance of the first order transition is consistent with the smoothing of the solid-liquid transition in single crystals as the density of defects is increased.

The appearance of a certain dissipation enables to define an irreversibility line distinguishing the solid from the liquid region in the phase diagram. The irreversibility line of this sample (experimentally obtained using the criteria $\rho(T_{irr}) = \frac{1}{1000}\rho_n$) together with the irreversibility line and the melting line of the YBa$_2$Cu$_3$O$_{7-\delta}$ single crystal is shown in figure 3.10. It is observed that the irreversibility line for the MTG-YBa$_2$Cu$_3$O$_{7-\delta}$ sample lays above the irreversibility line of the single crystal but close to its melting transition. This
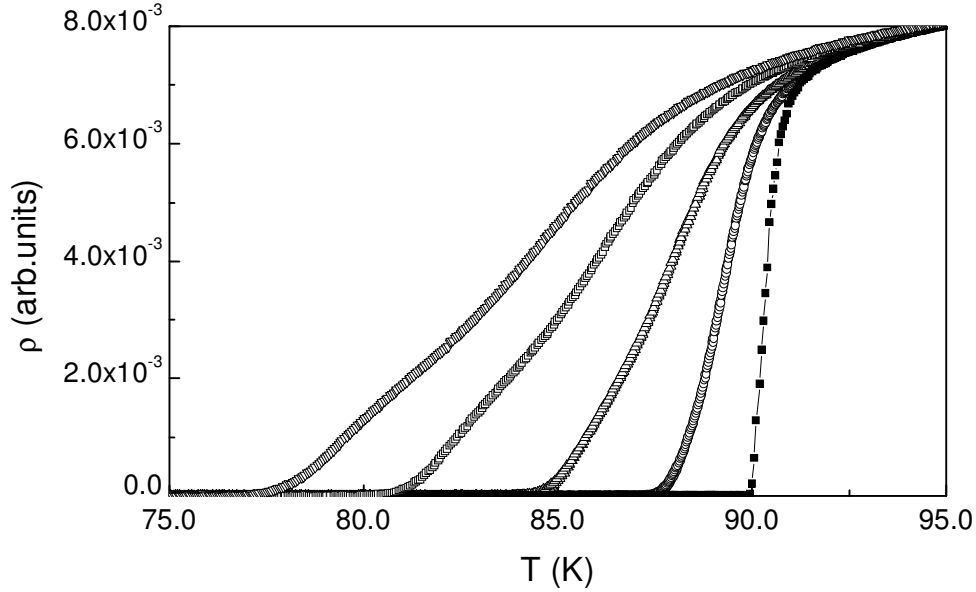
Figure 3.9: Resistive transitions at H=0T, 1T, 3T, 6T and 9T (H∥c) for a MTG-YBa$_2$Cu$_3$O$_{7-\delta}$ sample with 31% wt of Y$_2$BaCuO$_5$ particles.

evolution demonstrates that the introduction of a small amount of disorder breaks the vortex lattice and the onset of vortex motion appears at lower temperatures and therefore produces a downwards shift of the irreversibility line, as already shown [26]. At higher amounts of disorder (i.e. for the MTG-YBa$_2$Cu$_3$O$_{7-\delta}$ sample), the irreversibility line is shifted upwards due to the enhancement of vortex pinning. The irreversibility line for the MTG-YBa$_2$Cu$_3$O$_{7-\delta}$ sample, has been fitted to:

$$H_{irr} = H_0 \left(1 - \frac{T}{T_c} \right)^{\alpha} \tag{3.6}$$

obtaining H_0=165.8T and $\alpha = 1.5$. This value of α, for this sample is higher than that obtained for the temperature dependence of the melting line for the YBa$_2$Cu$_3$O$_{7-\delta}$ single crystal thus showing that the irreversibility temperature for the MTG-YBa$_2$Cu$_3$O$_{7-\delta}$ sample has a stronger dependence with the magnetic field. The exponent obtained for this MTG sample, and similarly to that observed for most of the samples studied in this work, is compatible with $\alpha = 1.5$ within the experimental error. Thus, we are able to relate the modifications of the value of H_0 with the differences observed in the microstructure.

Once obtained the field dependence of the irreversibility line, and considering the existence (for this particular direction of the magnetic field) of a certain influence of the twin boundaries, it reveals to be useful to rotate the magnetic field from the c-axis to the ab-plane in order to extract its influence. This procedure will be used through this thesis. The angu-
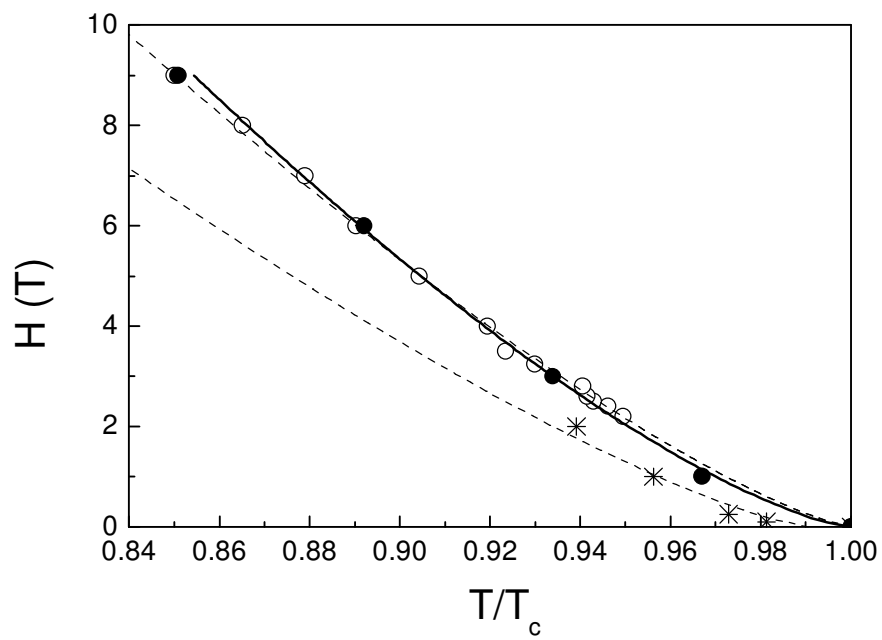
Figure 3.10: Irreversibility line for the sample with 31% wt Y_2BaCuO_5 particles ($\bullet$), together with the irreversibility line ($\star$) and the melting line ($\circ$) of the $YBa_2Cu_3O_{7-\delta}$ single crystal analyzed previously.
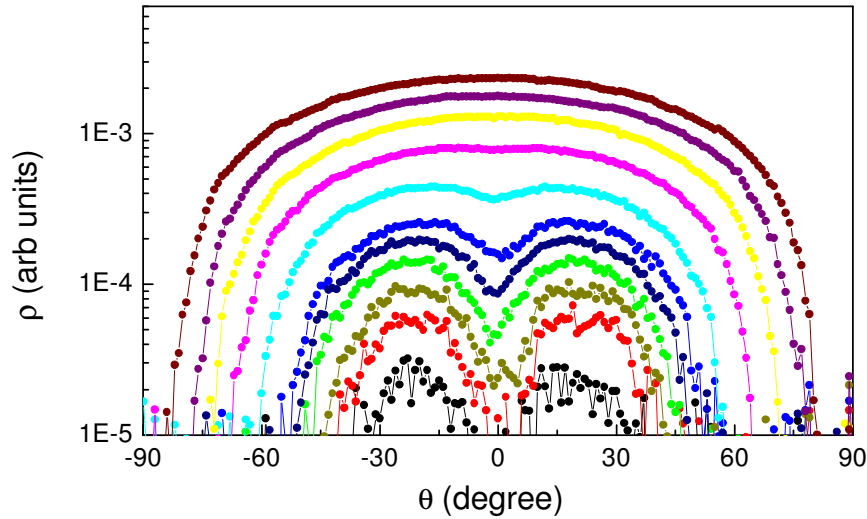
Figure 3.11: Angular dependence of the resistivity for different temperatures at H=3T for a MTG-YBa$_2$Cu$_3$O$_{7-\delta}$ sample with a 31% wt of Y$_2$BaCuO$_5$ particles.

lar dependence of the magnetoresistance measurements can be checked using two different experimental approaches:

1. Rotating the magnetic field at a fixed temperature, and

2. Measuring the temperature dependence of the resistivity at different orientations of the magnetic field.

Clearly, these two approaches are equivalent, since they both allow to explore the whole θ-T phase diagram, and will be used indistinctly in the following.

Figure 3.11 shows the angular dependence of the resistivity at different temperatures. Two different behaviors appear from this figure: at high temperatures, the resistivity of the sample increases as the direction of the applied field approaches the crystallographic c-axis, while, at lower temperatures the resistivity presents a dip for H∥c. The dip observed for H∥c has to be related to the enhanced vortex pinning at twin boundaries for this particular direction of the magnetic field. Twin boundaries, however, are not able to have an influence on vortex pinning for large deviations of the magnetic field with respect of the directions of twin boundaries. This non-monotonic behavior of the angular dependence of the resistivity enables to define the limit of the influence of twin boundaries, θ_{acc} (T), as the maximum in the ρ-θ curve. Once the influence of twin boundaries is avoided at high angles, the resistivity follows the intrinsic anisotropy of the sample and thus, the resistivity decreases when approaches the ab-plane.
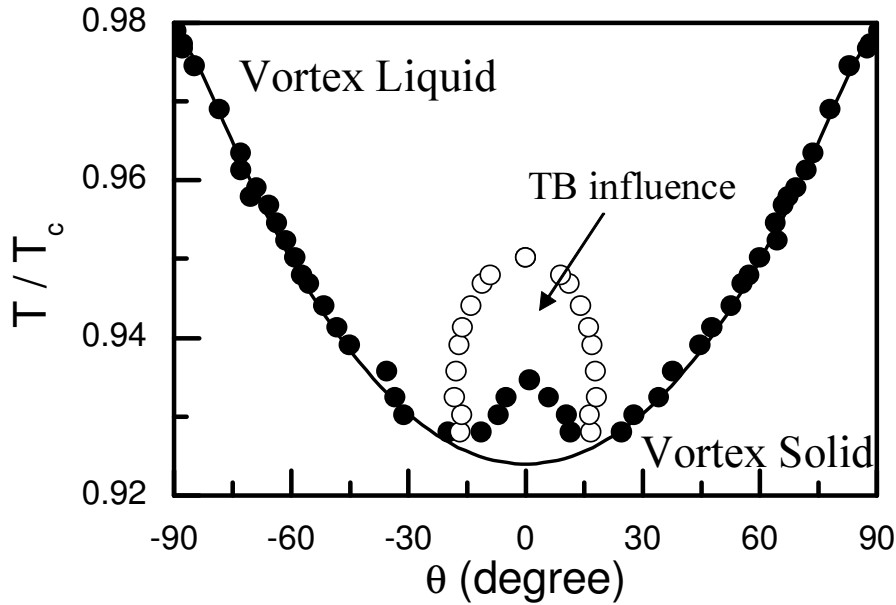
Figure 3.12: Angular dependent irreversibility line for the MTG-YBa$_2$Cu$_3$O$_{7-\delta}$ sample ($\bullet$) at H=3T . The limit of effectivity of twin boundaries ($\circ$) is also shown.

Therefore, these curves allow to distinguish three different regions present in the θ-T phase diagram (for each particular H chosen): a solid and a liquid vortex state (separated by the angular dependent irreversibility line) and the region with influence of twin boundaries over vortex motion. In figure 3.12 it is shown as representative data, the angular dependent phase diagram for H=3T. In this phase diagram are reflected the different behaviors of the angular dependent measurements (seen in figure 3.11):

- the anisotropic behavior of the resistivity, leading to a higher resistivity for H∥c than for H∥ab, promotes a similar anisotropic dependence of the irreversibility line, with an irreversibility temperature for H∥c lower than that of H∥ab.

- the dip in the resistivity near H∥c leads to a peak in the irreversibility temperature, and

- a region in the vortex liquid state located around H∥c with a certain influence of twin boundaries.

Similarly to what we observed for the single crystal, the anisotropic behavior of the angular dependent irreversibility line (for angles higher than θ_{acc}) is related to the anisotropy of the sample and follows equation 3.4, from where we obtain the fitting parameters: $\gamma^{-1} \approx 7$, α=1.6 and $H_0 = 61.72T$. It is remarkable that the anisotropic parameter γ^{-1} experimentally obtained for the YBa$_2$Cu$_3$O$_{7-\delta}$ single crystal and the MTG-YBa$_2$Cu$_3$O$_{7-\delta}$ sample are
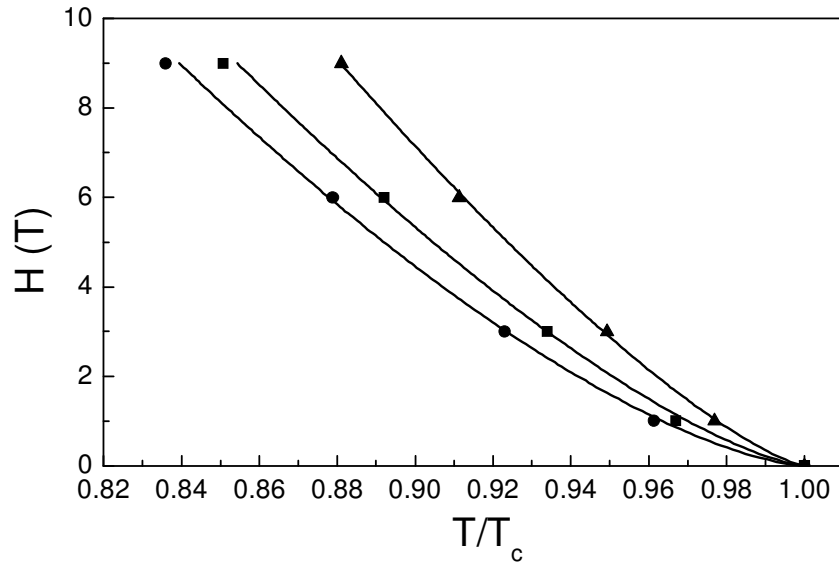
Figure 3.13: Magnetic Phase diagram for a MTG-YBa$_2$Cu$_3$O$_{7-\delta}$ sample with 31% wt of Y$_2$BaCuO$_5$. Shown are the irreversibility line (■), the irreversibility line without the influence of the twin boundaries (●) and the limit of effectivity of twin boundaries,T^* (▲).

similar, thus demonstrating that the anisotropy of the sample is neither influenced by the textured nature of the MTG sample nor by the presence of Y$_2$BaCuO$_5$ particles. Therefore, it is demonstrated that, as one may be expecting, the particular microstructure of the sample does not modify its intrinsic anisotropy. In the following section, we will show that angular dependent measurements are a sensible tool to detect modifications in the intrinsic anisotropy related to changes in the electronic structure of the material.

It is important to note that the fitting parameter α obtained from equation 3.4 differs from that obtained from equation 3.6 for the same sample, contrasting with the behavior observed in the single crystal, where the exponents steaming from equations 3.2, 3.3 and 3.4 are equal within the experimental error. The existence of this anomalous behavior, although unclear, might be attributed to the ceramic nature of these samples.

This angular dependent phase diagram may be constructed at several magnetic fields, thus enabling the obtention of the magnetic phase diagram for H∥c (see figure 3.13). This newly obtained phase diagram, compared with that of figure 3.10 incorporates additional curves determined through the angular dependence of this data: the irreversibility line where the influence of twin boundaries has been extracted and the limit of influence of twin boundaries on reducing vortex motion, T^*.

3.3.2   Vortex dynamics

Previously, we have observed that in the $YBa_2Cu_3O_{7-\delta}$ single crystal there is a wide region in the vortex liquid state where dissipation is consistent with the flux flow model. Now, we may wonder at which temperatures this region governed by flux flow motion is found in MTG-$YBa_2Cu_3O_{7-\delta}$ samples. In these samples, the higher microstructural complexity and density of defects suggests that the influence of vortex pinning is stronger, and therefore, the flux flow regime could vanish or be shifted to upper temperatures. To determine this region in MTG-$YBa_2Cu_3O_{7-\delta}$ samples, we proceed to analyze the already used angular dependent measurements, since they also enable us to determine whether vortex motion is controlled by flux flow or not.

Therefore, we used the temperature dependence of the resistivity at different directions of the magnetic field, since it provides a higher quantity of data, and therefore, the determination of its behavior becomes clearer. Following the same procedure than for the $YBa_2Cu_3O_{7-\delta}$ single crystal, we proceed by determining the ratio between the experimental data ($\rho(T)$) and the effective magnetic field, i.e. $\frac{\rho(T,B,\theta)}{B_{eff}}$ ($B_{eff} = \varepsilon_\theta \cdot B$), shown in figure 3.14. The observed behavior in this figure is, from a qualitative point of view, similar to that obtained for the single crystal once the effective magnetic field is considered: for any chosen temperature the value of this ratio is observed to saturate as the magnetic field approaches the c-axis (and the effective magnetic field that has to be considered increases). Thus the existence of a flux flow region, even in the complex MTG-$YBa_2Cu_3O_{7-\delta}$ samples, is strongly suggested.

This behavior of the measurements for the MTG-$YBa_2Cu_3O_{7-\delta}$ sample is further clarified in figure 3.15, where it is shown the angular dependence of the ratio $\frac{\rho}{B_{eff}}$ at different temperatures. In this figure, three different regions appear clearly:

1. At low temperatures and low angles, the value of the ratio $\frac{\rho}{B_{eff}}$ is reduced due to the presence of twin boundaries thus, enhancing vortex pinning.

2. At high angles, and low temperatures, there is still some influence of pinning, related to the high density of defects present in MTG-$YBa_2Cu_3O_{7-\delta}$ samples, and

3. At high temperatures and low angles, a region where the value of $\frac{\rho(T)}{B_{eff}}$ is almost independent of the effective magnetic field applied, thus suggesting that also in MTG-$YBa_2Cu_3O_{7-\delta}$ samples a region exists where vortex motion is consistent with flux flow. It is worth to note that, as one increases the temperature considered, the flux flow region expands to higher angles (and therefore, lower effective magnetic fields). This behavior is similar to that observed in figure 3.7, where the flux flow region expands to lower magnetic fields as the temperature is enhanced.

One must conclude, therefore, that, in spite of the strikingly different microstructure between single crystals and melt textured ceramic, there are important similarities between the superconducting properties of both families of samples:
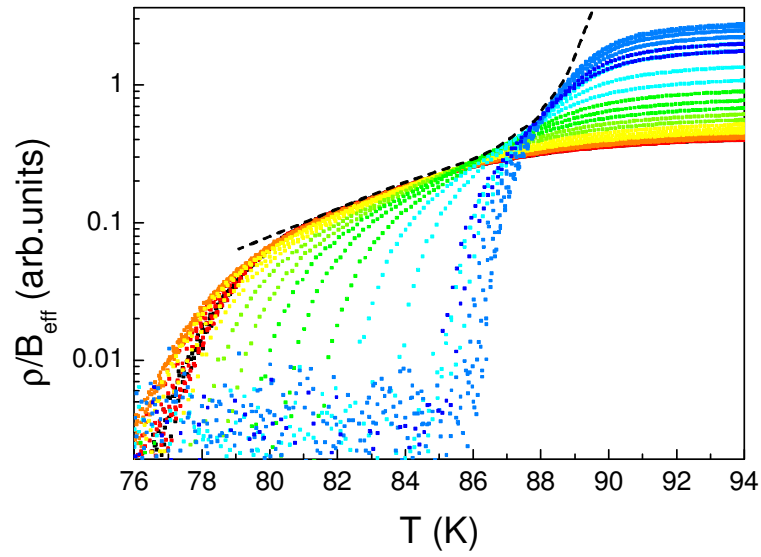
Figure 3.14: Temperature dependence of $\frac{\rho(T)}{B_{eff}}$ for H=9T. From black to blue, θ increases from 0 to 90 degree.
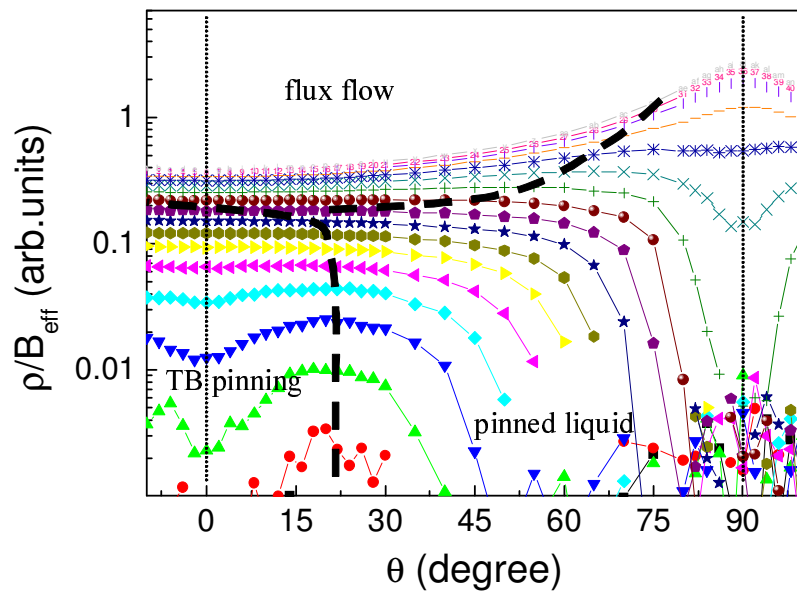

Figure 3.15: Angular dependence of $\frac{\rho(T)}{B_{eff}}$ for H=9T and different temperatures.

- A solid-liquid transition exists in both systems and it depends on the particular influence of disorder.

- A region near H∥c is observed where vortex motion is reduced by the presence of aligned defects such as twin boundaries.

- Once the influence of twin boundaries is extracted, angular dependent measurements show that the resistivity behaves anisotropically due to the intrinsic anisotropy of the sample. Furthermore, it has been observed that the anisotropic parameter γ^{-1} obtained for both systems is similar, in spite of the strong microstructural differences, thus demonstrating that the particular microstructure is not able to modify an intrinsic parameter like γ^{-1}.

- Finally, we have shown that in the phase diagram of both systems there exists a region at high temperatures and high magnetic fields where vortex motion is consistent with the flux flow model, and thus, it is not influenced by vortex pinning.

3.4   Related compounds

3.4.1   MTG-YBa$_2$(Cu$_{1-x}$Mg$_x$)$_3$O$_{7-\delta}$

The layered structure of high temperature superconductors is the main responsible of the electronic anisotropy, determined by the strength of the coupling between the conducting CuO$_2$ planes (see figure 1.5). Although in YBa$_2$Cu$_3$O$_{7-\delta}$ this coupling is strongly increased by the presence of the metallic Cu-O chains, the electronic structure of the planes is an essential item responsible of superconductivity. Therefore, the modification of the electronic structure of the CuO$_2$ planes reveals itself as a good method to investigate superconductivity and its origin in these systems.

In particular, the influence of the substitution of Cu at the CuO$_2$ planes by Ni or Zn has been extensively studied. It has been observed that a strong suppression of the superconducting properties, which is reflected, for instance, in a strong decrease of the critical temperature to values as large as $\frac{dT_c}{dx} \sim 12K/at\%$ for Zn[72]. Measurement of the local density of states by means of scanning tunnelling microscopy in layered materials have revealed that there is a local suppression of the superconductivity at the position of the impurity[73]. The origin of this suppression, however, is still under discussion.

Further insight into this mechanism can be performed by considering the atomic substitution of Cu by other atoms and compare their influence. At the Institut de Ciència de Materials de Barcelona, MTG-YBa$_2$Cu$_3$O$_{7-\delta}$ samples with different content of MgO have been obtained by adding to the standard starting mixture (69%wtYBa$_2$Cu$_3$O$_{7-\delta}$ + 30%wtY$_2$BaCuO$_5$ + 1%CeO$_2$) a certain amount of MgO (α%wt MgO, $0 \leq \alpha \leq 20\%wt$) [74–76]. The introduced MgO has been observed to partially incorporate into the crystalline structure, thus
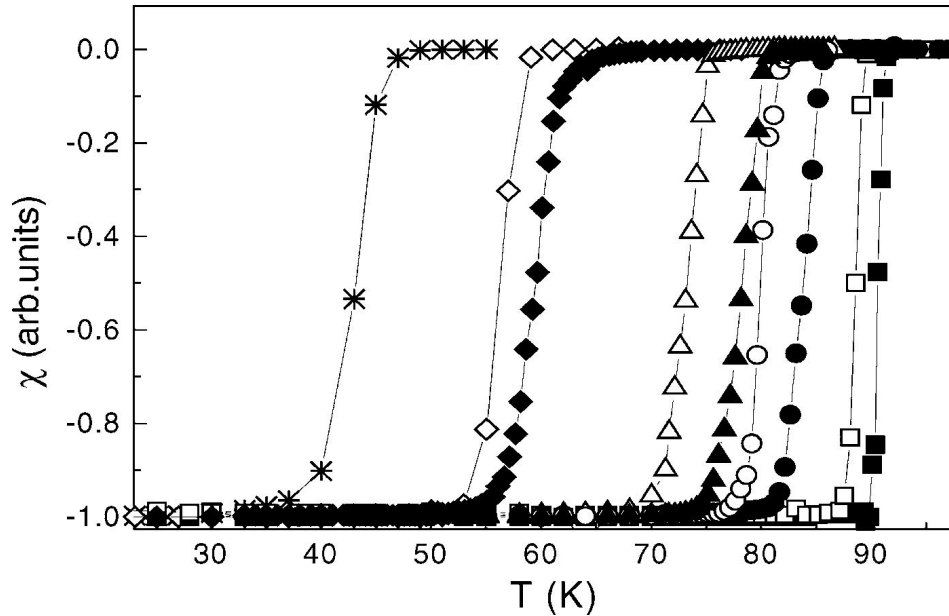
Figure 3.16: Magnetic transitions for MTG-$YBa_2Cu_3O_{7-\delta}$ samples + α MgO, with α = 0($\blacksquare$), 0.05($\square$), 0.1($\bullet$), 0.14($\circ$), 0.16($\blacktriangle$), 0.18($\triangle$), 0.5($\blacklozenge$), 1.0($\lozenge$) and 17($\star$)%wt.

forming $YBa_2(Cu_{1-x}Mg_x)_3O_{7-\delta}$, and enabling to determine the influence of Mg in the superconducting properties in general and the phase diagram in particular.

The magnetic transition for different contents of MgO is represented in figure 3.16, enabling to define the critical temperature as the midpoint of the superconducting temperature. It is observed that the superconducting transitions are strongly shifted downwards from T_c $\sim$90K to $T_c \sim 45$K, as increasing the content of MgO in the starting mixture, thus demonstrating the strong influence of doping, even at low contents of Mg.

The dependence of the critical temperature with α has been obtained and it is shown in figure 3.17. It is observed an initial linear decay of the critical temperature where one may assume a complete incorporation of Mg into the structure. At higher contents, the incorporation rate of Mg into the structure is slowed down and it is only partial, thus having a lower decrease of the critical temperature with the overall MgO content.

Following the assumption that (at low contents) there is a complete incorporation of Mg into the structure, we are able to transform the %wt content of MgO (α), into the atomic fraction of Mg (x) that has been incorporated into the structure of $YBa_2(Cu_{1-x}Mg_x)_3O_{7-\delta}$. In figure 3.17b, the temperature dependence of the critical temperature with the content of Mg in the atomic structure of $YBa_2(Cu_{1-x}Mg_x)_3O_{7-\delta}$ is shown and compared with that reported from the literature for $YBa_2Cu_3O_{7-\delta}$ samples doped with Zn. It is observed that both substitutions have the same decay rate of the critical temperature with the concentration, although the strong differences between both atoms (for instance, the ionic radius of Magnesium is
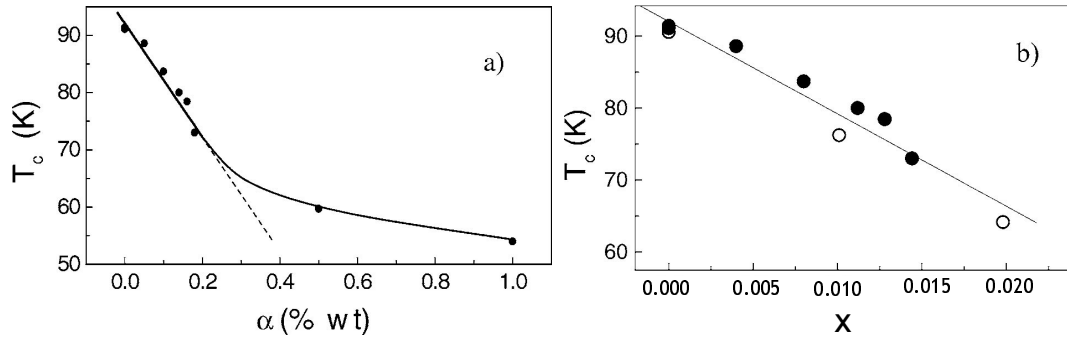
Figure 3.17: Dependence of the critical temperature (a) with the nominal content of MgO and (b) with the atomic content of Mg($\bullet$) or Zn ($\circ$).The data corresponding to the suppression of the critical temperature with Zn has been extracted from [72].

smaller than that of Zn: $r(Mg^{2+})$=0.65 Å and $r(Zn^{2+})$ =0.74Å).

If one extrapolates the observed linear dependence up to higher concentrations of Mg, the atomic content of Mg may be estimated from the experimental critical temperature. This simple estimation will enable us to correlate the observed superconducting temperatures with the actual content of Mg in the atomic structure.

In particular, the determination of the dependence of the anisotropy with x, in $YBa_2(Cu_{1-x}Mg_x)_3O_{7-\delta}$ and a subsequent comparison with that obtained in Zn may be useful to improve our understanding of the superconducting suppression with in-plane doping. As we have demonstrated in the last section, the study of the angular dependence of the irreversibility line enables to determine the intrinsic anisotropy of the superconducting systems.

To determine the angular dependent irreversibility line, we proceeded by measuring the angular dependent resistivity, for 4 different MTG-$YBa_2(Cu_{1-x}Mg_x)_3O_{7-\delta}$ samples with $0 < x < 0.04$. In figure 3.18, we observe the angular dependence of the resistivity in two different samples (at different conditions), which allows us to obtain the angular dependent irreversibility line. An important characteristic of the sample with the higher x is that, in the whole set of angular measurements performed in order to obtain the anisotropy of the sample, no evidence of pinning due to twin boundaries was found for H$\|$c, although twin boundaries were certainly observed by optical analysis. This lack of influence of the twin boundaries present in the sample, has also been reported in $ErBa_2Cu_3O_{7-\delta}$ [77], and it has been attributed to a reduced distortion of the atomic structure in this system as compared to that observed in $YBa_2Cu_3O_{7-\delta}$, where a distortion of the atomic positions across twin boundaries appears, as shown in figure 3.19. Certainly, it can not be concluded that this is the origin of the lack of influence that we have observed in the $YBa_2(Cu_{1-x}Mg_x)_3O_{7-\delta}$ sample, although it remains as a plausible explanation.

From the resistivity measurements, we are able to determine the angular dependent irreversibility line for these samples, which is shown for two of them at H=3T in figure 3.20.
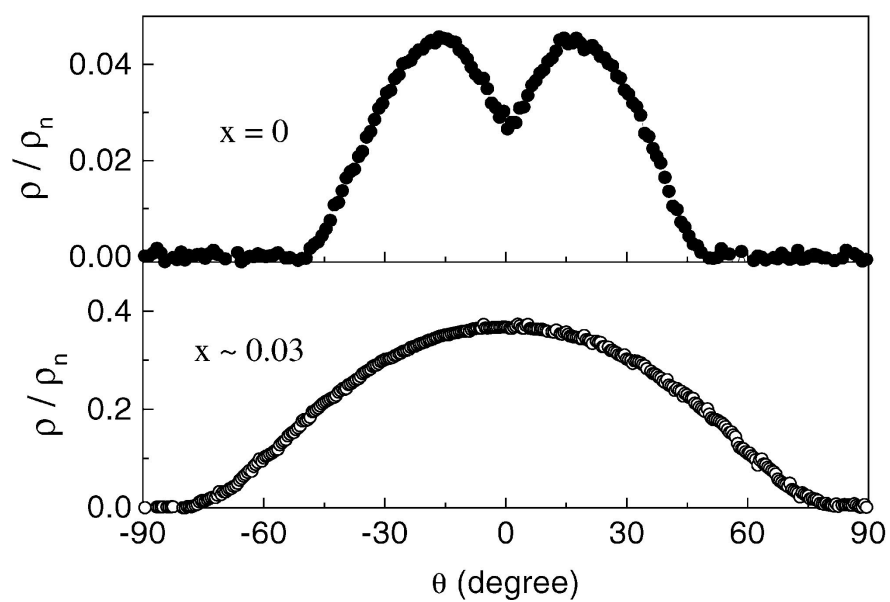
Figure 3.18: Anisotropic resistivity for x=0 ($\bullet$) and x$\sim$0.03($\circ$) YBa$_2$(Cu$_{1-x}$Mg$_x$)$_3$O$_{7-\delta}$ samples at H=3T and $\frac{T}{T_c} \approx 0.941$ and 0.945, respectively.
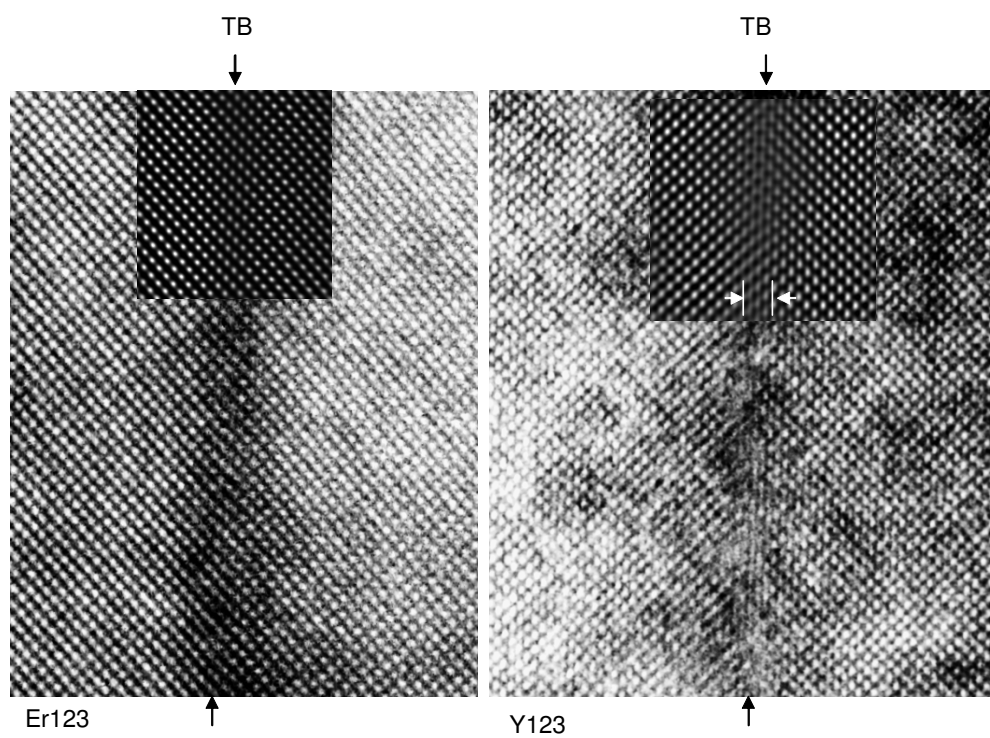
Figure 3.19: Image of a twin boundary obtained by High Resolution-Transmission Electronic Microscopy in left: anErBa$_2$Cu$_3$O$_{7-\delta}$ sample and right: a YBa$_2$Cu$_3$O$_{7-\delta}$ sample. [77]
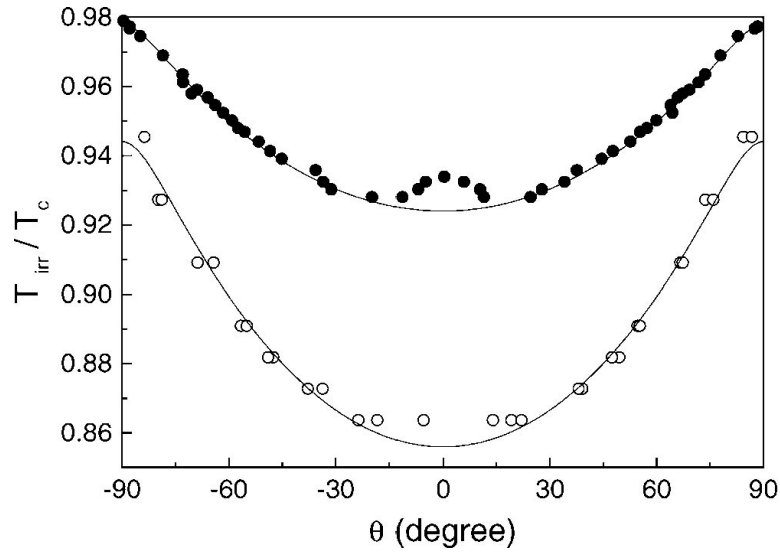
Figure 3.20: Angular dependent irreversibility line for two $YBa_2(Cu_{1-x}Mg_x)_3O_{7-\delta}$ samples with x=0 and x$\sim$ 0.03 at H=3T. The solid lines are the fit of the experimental data to equation 3.4.

First, it is observed that, as x increases, the angular dependent irreversibility line is shifted downwards and second, from the fit of these measurements (for angles without the influence of the twin boundaries) to equation 3.4 we found that the anisotropy of the system also decreases as the content of Mg increases.

Thus, a downwards shift of the irreversibility line is obtained as the anisotropy of the system decreases. This behavior is contrary to what one should expect when considering the scaling of the irreversibility line with the sample anisotropy (see 1.2.1). However, the introduction of Mg atoms into the atomic structure of $YBa_2Cu_3O_{7-\delta}$ may also have other consequences on the other superconducting properties, and they could be the responsible for this overall downwards shift of the irreversibility line. We have seen previously that equation 3.2 relates the position of the melting line with the intrinsic properties of the HTSC: $H_m(0) = \frac{c_L^4 \Phi_0^5 \gamma^2}{12\pi k_B^2 T_c^2 \mu_0^2 \lambda_{ab}^4}$. The critical temperature decreases from $T_c \sim 90K$ to $T_c \sim 45K$, and also does the anisotropy from $\gamma^{-1} \sim 7$ to $\gamma^{-1} \sim 4$. According to the theoretical expression of $H_m(0)$, $H_m(0)$ should lead to an upwards shift of the irreversibility line (in agreement with the scaling shown in figure 1.16), contrary to that observed. However, measurements of the a.c. susceptibility in Zn doped samples (with a contents of Zn similar to our limit of Mg and therefore, a similar critical temperature) reported an increase of the penetration depth larger than a factor of 2. Thus, if we consider the same enhancement in λ_{ab} for the sample with
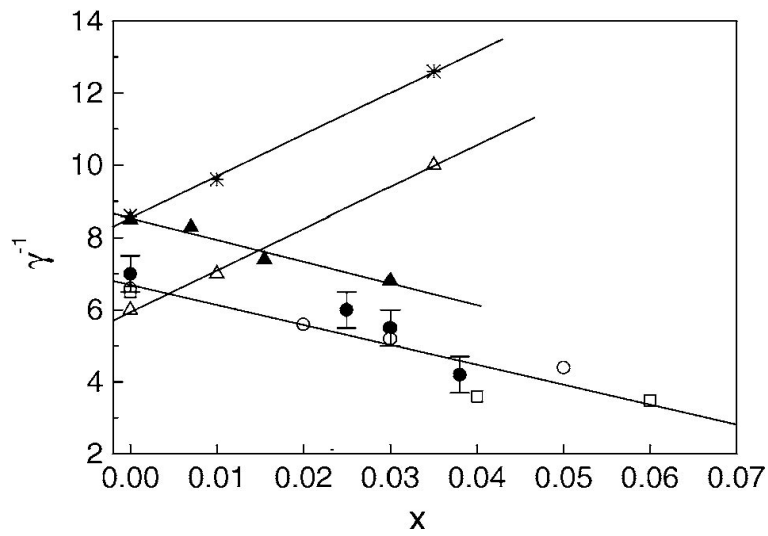
Figure 3.21: Dependence of the anisotropy of the system with the content of Mg for YBa$_2$(Cu$_{1-x}$Mg$_x$)$_3$O$_{7-\delta}$ samples (●). Also included for comparison purposes is the dependence on Zn substitution of YBa$_2$(Cu$_{1-x}$Zn$_x$)$_3$O$_{7-\delta}$ as determined by other authors: (○) from penetration depth measurements [78], (△) and (▲) from resistivity fluctuations[79] and [80] respectively, (□) from reversible magnetization [81] and (∗) from vortex glass transitions [82].

the higher content of MgO, an overall reduction of $H_m(0)$ about 50% is obtained, in good qualitative agreement to the experimental reduction observed.

3.4.2 MTG-NdBa$_2$Cu$_3$O$_{7-\delta}$

To further investigate the characteristics of vortex motion in systems with a structure similar to that of YBa$_2$Cu$_3$O$_{7-\delta}$, we decided to investigate a MTG sample of NdBa$_2$Cu$_3$O$_{7-\delta}$. Although the crystallographic structure of both systems is similar, the ionic sizes of Y and Nd are slightly different, being Nd slightly larger. Therefore, the NdBa$_2$Cu$_3$O$_{7-\delta}$ lattice is expanded compared to that of YBa$_2$Cu$_3$O$_{7-\delta}$. One important consequence of this expansion is a slight increase of T$_c$ up to T$_c \approx 95K$ which can lead to a remarkable increase of H$_{irr}$ at T=77K. Several authors have actually reported that $H_{irr}(77K) \approx 12T$. [83] However, the influence of this expansion on the intrinsic anisotropy is unknown.

Another important crystallographic difference between YBa$_2$Cu$_3$O$_{7-\delta}$ and NdBa$_2$Cu$_3$O$_{7-\delta}$ is that Nd is partially incorporated into the Ba site (see figure 1.5), forming the solid solution Nd$_{1+x}$Ba$_{2-x}$Cu$_3$O$_{7-\delta}$. This partial substitution may, indeed, have important consequences on the superconducting properties. It has been shown, particularly, that T$_c$ decreases with x, the amount of Nd substitution at the Ba site [84].

In order to investigate the possible influence of these modifications on superconducting properties, we proceeded by determining the magnetic phase diagram for both, H∥c and H∥ab. To do so, we measured the temperature dependence of the resistivity at different intensities of the applied magnetic field, which are shown in figure 3.22.

In this figure, it is observed that the superconducting transition takes place at temperatures higher than YBa$_2$Cu$_3$O$_{7-\delta}$. The larger critical temperature (T$_{c0}$=94.12K) of NdBa$_2$Cu$_3$O$_{7-\delta}$, is found to be in agreement with the values reported on the literature and increases as the ionic radius of the rare earth ion increases [85].

In the resistive transitions thus obtained, both for H∥c and H∥ab for Nd$_{1+x}$Ba$_{2-x}$Cu$_3$O$_{7-\delta}$ there is no signature of a first order transition, as we should have expected from the complex microstructure of MTG samples. Therefore, to continue investigating the superconducting properties of NdBa$_2$Cu$_3$O$_{7-\delta}$, we proceeded by determining the irreversibility line for both directions of the magnetic field, shown in figure 3.23, using the criterium $\rho(T_{irr}) = 1/1000\rho_n$. The irreversibility line for both directions of the magnetic field is shown in figure 3.23.

Similarly to YBa$_2$Cu$_3$O$_{7-\delta}$, the irreversibility line for H∥ab is found at temperatures much larger than those of H∥c, being a signature of the anisotropy of the sample. The particular value of the anisotropy, will be extracted from the angular dependence of the irreversibility line. However, the ratio between the fitting parameters H_0 for H∥ab and H∥c, allows us to obtain a rough estimate of the anisotropic factor $\gamma^{-1} \sim 6$, in good qualitative agreement with a result previously reported in the literature $\gamma^{-1} \approx 5.4$ [86], obtained with the same method.

We further proceed to investigate the whole angular dependent phase diagram by measuring the angular dependence of the resistivity at different applied fields, shown in figure 3.24. In this figure, it is observed that $\rho(\theta)$ measurements of MTG-NdBa$_2$Cu$_3$O$_{7-\delta}$ are qualita-
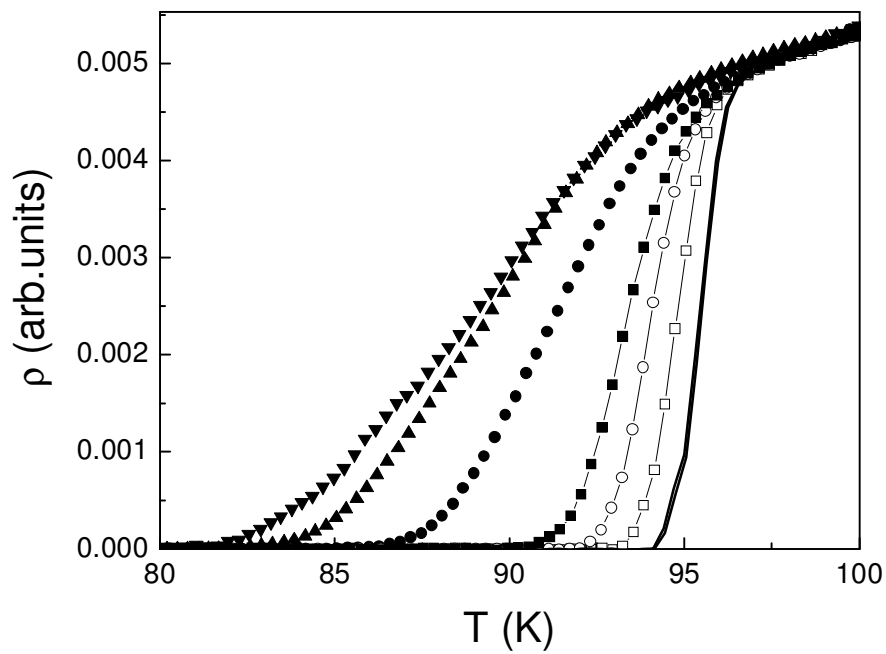
Figure 3.22: Temperature dependence of the resistivity, for H∥c (■,●, ▲ and) at H= 1,3, 4.5 and 6T and H∥ab (○, □) at H=1,3T. Also shown is the zero field transition.
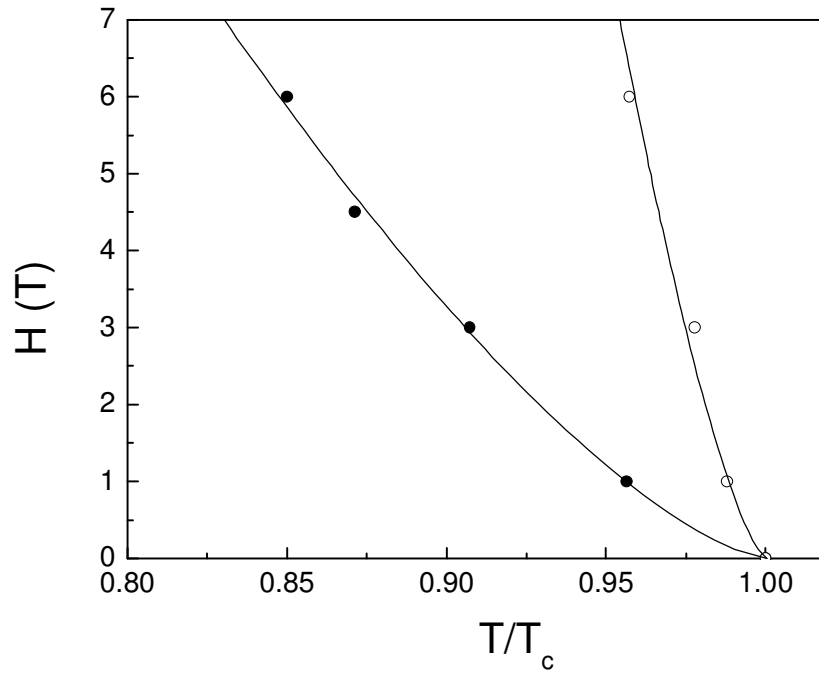
Figure 3.23: Magnetic phase diagram for a MTG-NdBa$_2$Cu$_3$O$_{7-\delta}$ sample. Shown are the irreversibility line for H∥c (●) and H∥ab (○).
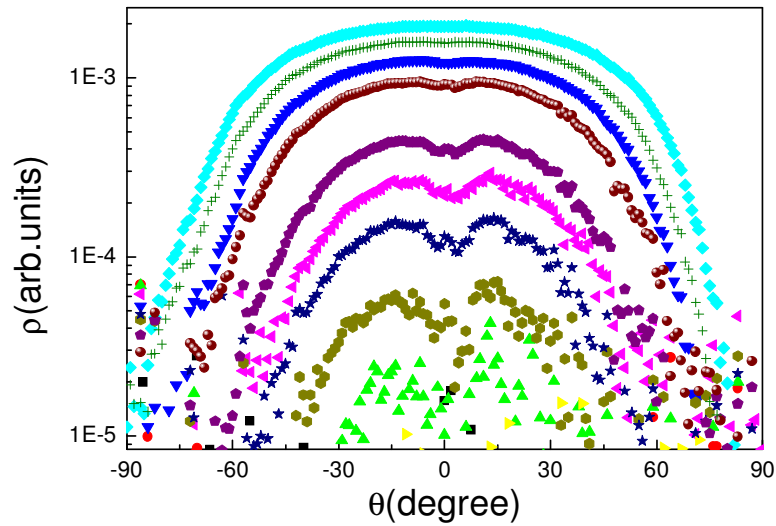

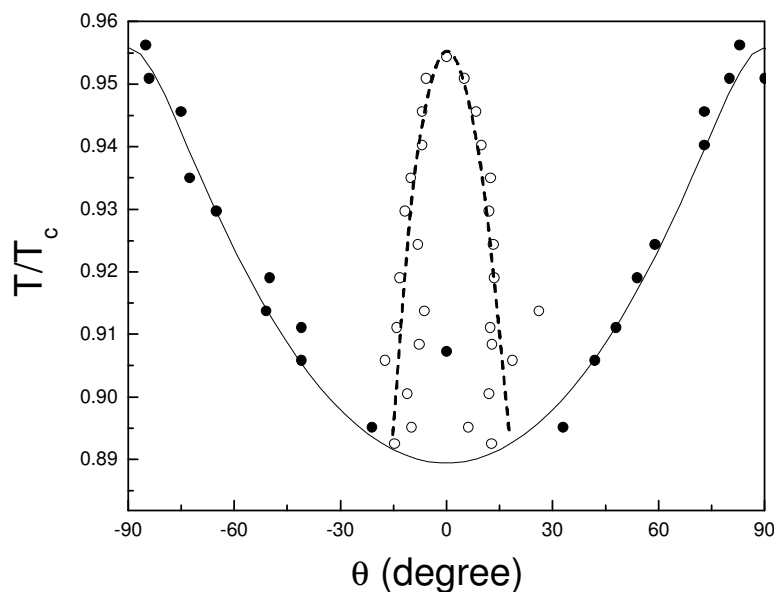Figure 3.24: Angular dependence of the resistivity for the Nd sample, for H=3T and different temperatures.

Figure 3.25: Angular dependent phase diagram for the MTG NdBa$_2$Cu$_3$O$_{7-\delta}$ sample at H=3T. Shown are the irreversibility line, $T_{irr}(\theta)$, (●) and the region of influence of twin boundaries, $T_{acc}(\theta)$, (○).

tively similar to those of the MTG-YBa$_2$Cu$_3$O$_{7-\delta}$ sample. Firstly, for angles near H∥c, a reduction of the resistivity is found. This reduction is analog to that observed in YBa$_2$Cu$_3$O$_{7-\delta}$, which is related to vortex pinning at twin boundaries. NdBa$_2$Cu$_3$O$_{7-\delta}$, is also orthorhombic (although the orthorhombicity is ∼ 10% lower [87]), and therefore introduces twin boundaries and thus modifies vortex pinning. Secondly, as the temperature is increased, a vortex liquid state starts to develop. At low temperatures, this liquid state is confined at directions close to H∥ab. Further increasing temperature, the liquid regions expands to the whole angular range.

The boundaries between the different regions previously defined in YBa$_2$Cu$_3$O$_{7-\delta}$ can also be defined in this case from angular dependent measurements leading to the phase diagram shown in figure 3.25. Similarly to what we have done previously, the experimental data of the angular dependent irreversibility line may be fitted to equation 3.4, from where the mass anisotropy ratio is extracted. A value of $\gamma^{-1} \approx 4.7$ is thus obtained, slightly smaller than the values reported for YBa$_2$Cu$_3$O$_{7-\delta}$, $\gamma^{-1} \approx 7$. From a qualitative point of view, this lower anisotropy of NdBa$_2$Cu$_3$O$_{7-\delta}$ compared to that of YBa$_2$Cu$_3$O$_{7-\delta}$ would require a significative reduction of the spacing between CuO chains and CuO$_2$ layers, which has not been observed, up to our knowledge. In this figure it is also shown the region of influence of twin boundaries, that has also a qualitative behavior similar to that observed in YBa$_2$Cu$_3$O$_{7-\delta}$: the
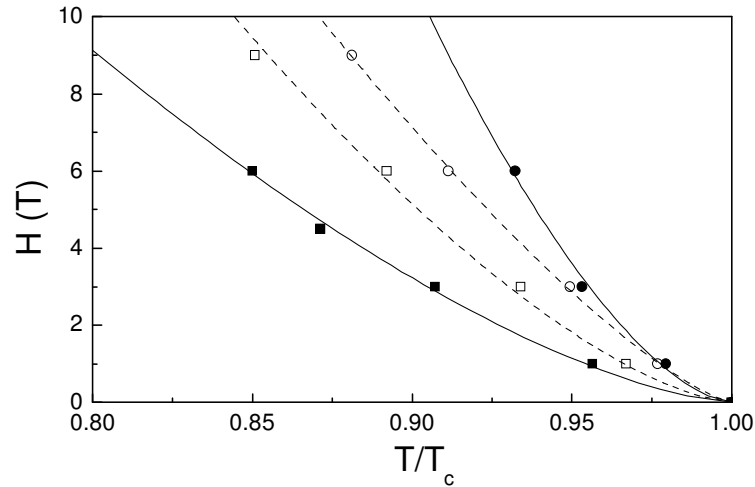
Figure 3.26: Magnetic phase diagram for H∥c. Shown is the irreversibility line (■, □) and the limit of influence of twin boundaries, T^* (●, ○) for $YBa_2Cu_3O_{7-\delta}$ (○,□) and $NdBa_2Cu_3O_{7-\delta}$ (●, ■).

accommodation angle (θ_{acc} (T)) monotonically reduces and ends up at a certain temperature (T*) and thus enables to define the magnetic phase diagram for H∥c.

The dependence of T* with the magnetic field is shown in figure 3.26, together with the irreversibility line (with the influence of twin boundaries). For comparison, the same curves for the sample analyzed in section 3.3 are shown. Although it has to be noted that a quantitative comparison is not possible due to the microstructural differences existing between both samples, it appears clearly that:

- The irreversibility line for $NdBa_2Cu_3O_{7-\delta}$ is shifted downwards. This is contrary to the expected behavior (and the results obtained from the literature) if we take into account the lower anisotropy of $Nd_{1+x}Ba_{2-x}Cu_3O_{7-\delta}$. As it will be discussed thorough this thesis, the microstructure of the sample modifies the position of the irreversibility line, and therefore a modification of the concentration of pinning centers or defects having a detrimental effect on the irreversibility line can originate the observed shift.

- The limit of influence of twin boundaries for the $NdBa_2Cu_3O_{7-\delta}$ sample is found at temperatures higher than that of the $YBa_2Cu_3O_{7-\delta}$ sample. This is an interesting result which will be further discussed in chapter 8 where an unified analysis of the relationship among anisotropy and the superconducting vortex liquid phase diagram will be performed.

3.5   Conclusions

In this chapter, different systems have been analyzed by means of magnetoresistance measurements. We have investigated the properties of the vortex liquid state of a twinned, clean, YBa$_2$Cu$_3$O$_{7-\delta}$ single crystal and a MTG-YBa$_2$Cu$_3$O$_{7-\delta}$ sample. It has been shown that, in spite of the strong microstructural differences, important similarities still exist:

- An upwards shift of the irreversibility line for H$\|$c and thus, magnetic fields parallels to twin boundaries.

- The angular dependent irreversibility line follows the intrinsic anisotropy of the system and the obtained anisotropic parameter γ^{-1} is similar for both systems.

- A region in the vortex liquid phase diagram is found where vortex motion is consistent with the flux flow model.

We have also investigated the influence of Mg doping in MTG-YBa$_2$(Cu$_{1-x}$Mg$_x$)$_3$O$_{7-\delta}$. It has been shown that Mg doping promotes a decrease of the anisotropy and a downwards shift of the irreversibility line. This downwards shift could be related to the modification of the intrinsic properties of YBa$_2$(Cu$_{1-x}$Mg$_x$)$_3$O$_{7-\delta}$, thus, reducing the strength of vortex pinning in this system. Finally, the superconducting properties of NdBa$_2$Cu$_3$O$_{7-\delta}$ have been studied. The strong decrease of the anisotropy observed in this sample is consistent with the strong upwards shift of the irreversibility line reported in the literature.